MARS GLOBAL SURVEYOR THERMAL EMISSION SPECTROMETER (TES) OBSERVATIONS: ATMOSPHERIC TEMPERATURES DURING AEROBRAKING AND SCIENCE PHASING

Barney J. Conrath
Center for Radiophysics and Space Research
Cornell University, Ithaca, NY 14853

John C. Pearl, Michael D. Smith, and William C. Maguire
NASA/Goddard Space Flight Center
Greenbelt, MD 20771

Philip R. Christensen
Department of Geology, Arizona State University
Tempe, AZ 85287

Shymala Dason
Solutio Internet Guides
Laurel, MD 20724

Monte S. Kaelberer
Raytheon ITSS
Lanham, MD 20706

Submitted to *Journal of Geophysical Research*

Send correspondence and proofs to:

Barney J. Conrath

11805 Haven Hill Dr.

Smithsburg, MD 21783

e-mail: barney@chryse.gsfc.nasa.gov

voice and fax: 301-824-6076

ABSTRACT

Between September 1997, when the Mars Global Surveyor spacecraft arrived at Mars, and September 1998 when the final aerobraking phase of the mission began, the Thermal Emission Spectrometer (TES) has acquired an extensive data set spanning approximately half of a Martian year. Nadir-viewing spectral measurements from this data set within the 15-μm CO_2 absorption band are inverted to obtain atmospheric temperature profiles from the surface up to about the 0.1 mbar level. The computational procedure used to retrieve the temperatures is presented. Mean meridional cross sections of thermal structure are calculated for periods of time near northern hemisphere fall equinox, winter solstice, and spring equinox, as well as for a time interval immediately following the onset of the Noachis Terra dust storm. Gradient thermal wind cross sections are calculated from the thermal structure. Regions of possible wave activity are identified using cross sections of rms temperature deviations from the mean. Results from both near-equinox periods show some hemispheric asymmetry with peak eastward thermal winds in the north about twice the magnitude of those in the south. The results near solstice show an intense circumpolar vortex at high northern latitudes and waves associated with the vortex jet core. Warming of the atmosphere aloft at mid-northern latitudes suggests the presence of a strong cross-equatorial Hadley circulation. Although the Noachis dust storm did not become global in scale, strong perturbations to the atmospheric structure are found, including an enhanced temperature maximum aloft at high northern latitudes resulting from intensification of the Hadley circulation. TES results for the various seasonal conditions are compared with published results from Mars general circulation models, and generally good qualitative agreement is found.

1. INTRODUCTION

The Thermal Emission Spectrometer (TES) carried on the Mars Global Surveyor spacecraft consists of a Michelson interferometer, along with solar albedo and broadband thermal channels (Christensen et al., 1992). The spectrometer measures thermal emission between 200 and 1600 cm^{-1} with selectable nominal spectral resolutions of 5 and 10 cm^{-1}. The individual pixels of the 2×3 detector array subtend 8.3 mrad. A pointing mirror permits the nadir as well as the forward and aft limbs to be viewed. Calibration of the instrument is accomplished with periodic views of an on-board blackbody and cold space. Although the primary objectives of the experiment are related to surface science, the thermal emission spectra also contain a wealth of information on various atmospheric parameters including thermal structure, water vapor, and aerosols (dust and condensates).

Thermal emission measurements from spacecraft have been extensively used to obtain temperature profiles in terrestrial meteorological satellite programs, and the approach has also been applied to the atmospheres of other planets including Mars. In the case of Mars, measurements within the CO_2 absorption band complex centered at 667 cm^{-1} (15 μm) are used. Mariner 9 IRIS spectra were inverted to obtain temperatures during the 1971 global dust storm and its subsequent dissipation (Hanel et al., 1972; Conrath et al., 1973; Conrath, 1975; 1976; 1981; Santee and Crisp 1993). The Viking IRTM obtained extensive information on the mean temperature of a thick atmospheric layer from a single–channel, broadband measurement in the CO_2 band (Martin and Kieffer, 1979; Martin, 1981; Jakosky and Martin, 1987). Temperature profiles not only provide diagnostic information on the dynamics and energetics of the atmosphere, they are the essential starting point for the retrieval of all other atmospheric parameters from thermal emission spectra, and for the isolation of emission from the planetary surface (Smith et al., 1999a; Bandfield et al., 1999).

During the time between the arrival of MGS at Mars in September 1997 and September 1998, over 2 million temperature profiles were retrieved. These were primarily obtained from nadir–viewing spectra, with a limited number of profiles retrieved from limb spectra acquired near periapsis. Only nadir retrievals are presented here; limb retrievals will

be treated in future work. Slightly more than one half of a Martian seasonal cycle was observed during this period of time, extending from just after northern hemisphere autumnal equinox, through winter solstice, and into northern hemisphere spring (L_s = 184–28, where L_s is the areocentric longitude of the sun). Several regional dust storms occurred during this period, the largest of which was the Noachis Terra event in late November 1997 (Christensen et al., 1998; Smith et al., 1999b). The TES retrievals provide the most extensive spatial and temporal coverage yet obtained for this portion of the Martian seasonal cycle. A set of temperature profiles have also been obtained from MGS radio occultation measurements (Hinson, et al., 1999), and the two data sets should prove to be highly complimentary. While more limited in spatial and temporal coverage, the occultation profiles possess high vertical resolution, and also directly provide pressure as a function of geopotential. The objectives of this paper are to describe the computational approach used to retrieve temperature profiles from TES spectra and to present selected examples of the results, illustrating the seasonal evolution of the mean atmospheric thermal structure and the associated thermal winds. Temperature variances are included as possible indicators of wave activity. The results presented here are based on preliminary retrievals that are subject to future refinements.

The temperature profile retrieval algorithm used in the analysis is presented in Section 2. Selection of the data sets used is discussed in Section 3. In Section 4, the results are presented, and their implications for Martian atmospheric dynamics are discussed. Finally, our conclusions are summarized in Section 5.

2. TEMPERATURE RETRIEVAL ALGORITHM

Measurements of thermal emission within an absorption band associated with a constituent of known abundance can be used to estimate temperature as a function of atmospheric pressure level. Radiances near the opaque band center are sensitive to the upper atmospheric levels while those in the more nearly transparent band wings provide information on layers nearer the planetary surface; on Mars, the CO_2 band complex centered at 667 cm^{-1} is well-suited for this purpose. The quantitative approach used to retrieve thermal structure from TES measurements within this band is summarized in this section.

The thermal spectral radiance $I(\mu, \nu)$ emerging from the top of the atmosphere as measured at the spacecraft can be written

$$I(\mu,\nu) = \epsilon(\nu)B(\nu,T_s)Tr(\mu,\nu,z_s) + \int_{z_s}^{z_t} B[\nu,T(z)]\frac{\partial Tr(\mu,\nu,z)}{\partial z}dz \qquad (1)$$

where μ is the cosine of the emission angle, ν is wavenumber, $z = -\ln p$ where p is atmospheric pressure, $Tr(\mu, \nu, z)$ is atmospheric transmittance from level z to the top of the atmosphere, and $B(\nu, T)$ is the Planck radiance at wavenumber ν and temperature T. The first term represents the atmospheric attenuated emission from the planetary surface with emissivity $\epsilon(\nu)$ and temperature T_s. The second term is the atmospheric emission contribution with the integral taken from the surface z_s to the effective "top" z_t above which contributions to the outgoing radiance are negligible. In writing (1), scattering has been neglected and the atmosphere is assumed to be in local thermodynamic equilibrium at all levels. We have also neglected a term representing upward reflection by the surface of downward thermal flux from the atmosphere, a term that will generally be small as long as $\epsilon(\nu)$ does not differ greatly from unity.

The direct retrieval of temperature from (1), given measurements of $I(\mu, \nu)$, is an "ill-posed" problem in the sense that arbitrarily small changes in the measured radiances can produce finite changes in the retrieved temperature profile, resulting in a hypersensitivity to measurement uncertainties. In addition, the problem will be underdetermined since the number of quadrature points for which the temperature must be specified will usually exceed the number of independent pieces of information contained in the radiance measurements. Nevertheless, it is possible to obtain physically meaningful solutions by imposing additional constraints that usually take the form of low-pass filtering, either explicitly or implicitly. An extensive discussion of this general type of inverse problem has been given by Craig and Brown (1986). There are several different approaches that could be applied to the problem at hand. The algorithm we have chosen is briefly summarized below and has been described in greater detail by Conrath et al. (1998).

We begin by using the numerical quadrature analog of (1) such that $T(z)$ is defined at n discrete atmospheric levels. Linearizing the resulting set of equations about a reference temperature profile $T^0(z)$ yields

$$\mathbf{\Delta I} = K\mathbf{\Delta T} \tag{2}$$

where K_{ij} is the functional derivative of the radiance at ν_i with respect to T at level z_j. The perturbation quantities are

$$\Delta T_j = T(z_j) - T^0(z_j), \tag{3}$$

$$\Delta I_i = I(\nu_i) - I^0(\nu_i), \tag{4}$$

where the radiance $I^0(\nu_i)$ is calculated using T^0. Let $\mathbf{\Delta T}$ be expanded in a set of basis vectors, i.e.,

$$\mathbf{\Delta T} = F\mathbf{a}, \tag{5}$$

where F is a matrix whose columns are the basis vectors, and the vector $\mathbf{a}$ contains the expansion coefficients. The solution we seek results from minimization with respect to $\mathbf{a}$ of the quadratic function

$$Q = (\mathbf{\Delta I} - KF\mathbf{a})^T E^{-1}(\mathbf{\Delta I} - KF\mathbf{a}) + \gamma \mathbf{a}^T\mathbf{a}. \tag{6}$$

Here, E is the measurement error covariance matrix. The first term on the right hand side of (6) is the usual penalty function employed in least squares fitting. In the second term, $\mathbf{a}^T\mathbf{a}$ is a measure of the departure of the solution from the reference or first guess profile, and the parameter γ determines the relative weight with which this constraint is applied. Carrying out the minimization and making use of (5) gives

$$\mathbf{\Delta T} = W\mathbf{\Delta I}, \tag{7}$$

where

$$W = SK^T(KSK^T + \gamma E)^{-1}. \tag{8}$$

$S = FF^T$ is the two-point correlation matrix of the basis vectors; only this parameter appears in the solution and not the basis vectors themselves. The nonlinearity of the problem is taken into account through iterative application of (7). The error covariance matrix for the retrieved temperature profile due to instrument noise propagation is

$$V = WEW^T. \tag{9}$$

The functional derivatives of radiance with respect to temperature are calculated assuming that the temperature dependence of the atmospheric transmittance is weak relative to that of the Planck function so that K can be approximated as

$$K_{ij} = \frac{\partial B[\nu_i, T(z_j)]}{\partial T_j} \frac{\partial Tr(\mu, \nu_i, z_j)}{\partial z_j}. \tag{10}$$

A set of functional derivatives (also referred to as contribution functions or kernels) for the wavenumbers chosen for the present study are shown in Fig. 1. These correspond to the nominal 10 cm^{-1} spectral resolution, and points on both sides of the 15-μm CO_2 band are included. Rapid calculation of atmospheric transmittance is required for temperature retrieval from a large volume of spacecraft measurements, and the k-distribution method (Goody et al. 1989) is used for this purpose.

In general, the correlation matrix S is a measure of the completeness of the set of basis vectors; for a complete set, it is proportional to the unit matrix. In the present application, we wish to limit the vertical scales represented in the solution to those intrinsic to the radiance measurements, and S provides a convenient means of filtering the solution. Rather than specifying a specific set of basis functions, we shall specify S to be of the form

$$S_{ij} = exp[-(z_i - z_j)^2/2c^2] \tag{11}$$

where c is the correlation length in scale heights, and can be regarded as a measure of the width of the numerical filter imposed on the solution by the retrieval algorithm. Based on estimates of vertical resolution from the behavior of K, a value of $c = 0.75$ is found to be appropriate. The parameter γ controls the strength of the filtering imposed on the solution, and is most easily determined through numerical experiment.

The measurement error covariance matrix can be written

$$E_{ij} = N^2\delta_{ij} + \epsilon(\nu_i)\epsilon(\nu_j)\frac{\partial B(\nu_i, T_s)}{\partial T}\frac{\partial B(\nu_j, T_s)}{\partial T}Tr(\mu, \nu_i, z_s)Tr(\mu, \nu_j, z_s) < \delta T_s^2 > \quad (12)$$

where N is the noise equivalent spectral radiance of the TES instrument, assumed to be constant within the spectral interval used, and $< \delta T_s^2 >$ is the statistical error in the required surface temperature determination. Since the random noise in the TES measurements is assumed to be uncorrelated between any two spectral points, the first term in (12) contains contributions to only the diagonal elements of E. However, errors in the determination of T_s affect all wavenumbers, resulting in correlations and off-diagonal elements as indicated by the second term.

To carry out an atmospheric temperature retrieval, the boundary term in (1) must be specified, and this can prove challenging. The surface pressure is required for calculation of the total atmospheric transmittance. In the analysis presented here, this quantity was estimated from a topographic map (U.S. Geological Survey, 1993), using a seasonally adjusted reference pressure based on Viking lander observations (Tillman et al., 1993). It is assumed that the surface emissivity $\epsilon(\nu)$ is unity throughout the spectral region containing the CO_2 band. While this may not be strictly true, the approach used in specifying T_s compensates for any departure from unity to first order. Rather than trying to define a surface temperature from the most transparent portions of the spectrum, we estimate an effective surface temperature by calculating brightness temperatures in narrow spectral regions on either side of the CO_2 band and averaging them. The wavenumber intervals used are 507.89–529.05 cm^{-1} and 804.15–825.31 cm^{-1}. In addition to compensating for emissivities less than unity, this approach also compensates for neglected dust opacity through first order in dust optical depth.

To begin each retrieval, an initial reference or "first guess" profile must be specified. Because of the large spatial and temporal variations in the Martian temperature profiles, it is necessary to use the measurements themselves to estimate a first guess. For each spectral radiance used in the inversion, brightness temperatures $T_B(\nu_i)$ are calculated using

$$B[T_B(\nu_i)] = \frac{I(\nu_i) - B(\nu_i, T_s)Tr(\nu_i, z_s)}{1 - Tr(\nu_i, z_s)} \tag{13}$$

These temperatures are assigned to effective atmospheric levels defined by

$$z_{eff}(\nu_i) = \sum_{j=1}^{n} K_{ij} z_j / \sum_{j=1}^{n} K_{ij}. \tag{14}$$

The resulting temperature profile is then interpolated between levels and extrapolated above the uppermost point to high atmospheric levels by assuming $T \propto p^{0.02}$. Finally, the profile is subjected to smoothing by convolution with a triangular window with a width of 0.75 scale height. This last step is to eliminate high spatial frequency components that would be retained in the retrieved solution as artifacts. Using a first guess profile defined in this way, it is found that the radiance residuals converge to near the noise level within three iterations.

The functional derivatives or contribution functions of Fig. 1 show that for the nominal 10 cm^{-1} spectral resolution and normal viewing ($\mu = 1$), maximum information on the atmospheric thermal structure is obtained from levels between the surface and about 0.3 mbar; above this level, the information content of the measurements gradually decreases. As the emission angle increases, the maxima of the contribution functions move upward (toward lower pressures). In this analysis, emission angles were limited to 60° ($\mu = 0.5$) for which the pressure level of the peak of the uppermost contribution function is about 0.2 mbar. To examine the capabilities and limitations of the retrieval algorithm, it was applied to synthetic spectra calculated from model Martian atmospheres, and the results for two such cases are shown in Fig. 2. The warm, relatively smooth profile in Fig. 2a is well recovered in the region of maximum information content. At higher atmospheric levels where the information decreases, the retrieval tends toward the first guess profile with the type of algorithm used here. The profile in Fig. 2b displays a strong inversion above the surface as might be found in early morning and in polar regions on Mars. The scale of the inversion structure lies below the intrinsic vertical resolution of the measurements and only its average properties are recovered.

There are several sources of uncertainty that contribute to errors in the retrieved

temperatures. The random errors in the retrieval due to propagation of measurement noise are characterized by the temperature error covariance matrix V (eq. (9)). An example of the structure of this matrix is shown in the form of a contour plot in Fig. 3. The square root of the diagonal elements of V are the rms errors at each level in the retrieved profile due to instrument noise propagation. The off-diagonal elements are measures of the correlation of the retrieval errors between each pair of atmospheric levels. The patterns of these correlations reflect the behavior of the overlapping contribution functions and the smoothing imposed by the retrieval algorithm. The right hand panels in Figs. 2a and 2b show the estimated rms statistical error in the retrievals due to propagation of instrument noise corresponding to a noise equivalent radiance of 2×10^{-8} W cm^{-2}ster^{-1}/cm^{-1}. Errors in the estimated surface pressures probably dominate the temperature retrieval uncertainty in the lowest part of the atmosphere over relatively warm surfaces. A surface pressure error of $\pm 5\%$ propagates into errors in the retrieved temperatures in the lowest layers of $\pm$1-6 K for surface temperatures of 200-260 K respectively. These errors decrease rapidly with increasing height, becoming negligible above about one pressure scale height. Also included among the possible sources of error are the radiometric calibration of the instrument, the assumption of unit surface emissivity, and the neglect of dust opacities. The use of an effective surface temperature to define the continuum for the 15-μm CO_2 band, as discussed above, partially compensates for the latter two effects as long as the surface emissivity does not depart significantly from unity and the dust opacity is small. Errors in the absolute radiometric calibration affect the retrievals most strongly under cold atmospheric and surface conditions. With the preliminary calibration of the data used in this analysis, systematic errors in excess of 5 K are possible in the cold winter polar regions; this is evident in some of the results presented below where the retrieved temperatures lie below the CO_2 condensation temperature. Uncertainties in the CO_2 absorption coefficients can also introduce systematic errors into the retrievals; the magnitude of these errors is not well known, but is probably less than 2 K.

3. DATA SELECTION

The TES data analyzed in this study are selected from data taken during the initial

aerobraking period from September 1997 to March 1998 and the "science phasing" portion of the mission from March to September 1998 when final aerobraking was initiated. During this time, the MGS spacecraft was in a highly elliptical orbit about Mars with an initial period of 45 hours, decreasing during the first aerobraking period to an 11.6 hour period, which remained fixed during science–phasing. Consequently, the projection of an individual TES pixel on the planet varied greatly from less than 10 km near periapsis to several hundred km near apoapsis. During this period, periapsis latitude moved northward from 32 N, passing over the north pole and then moving back to 61 N by the end of the science–phasing period. During the portion of the orbit near periapsis, most TES data were taken with the instrument pointed toward the nadir. Exceptions to this include a limited amount of limb data, not discussed in the present work. Following the periapsis pass, the roll of the spacecraft, combined with the use of the TES pointing mirror, permitted more extensive mapping of the planet to be achieved, but at lower spatial resolution. As a result, coverage in the northern hemisphere from a single orbit is largely confined to two regions about 180° and 12 hours apart in longitude and local time, while at high southern latitudes, more nearly complete coverage in longitude and local time is achieved.

Preliminary temperature retrievals have been obtained by inversion of almost all of the spectra acquired during the initial aerobraking and science–phasing portions of the mission, amounting to over 2 million temperature profiles. We wish to select subsets of these results that can be used to characterize the evolution of the thermal structure and associated thermal wind field during the approximately one half Martian year covered by the data thus far.

The temporal behavior of the 0.3 mbar temperatures at 30 N and 30 S is shown in Fig. 4. Superposed on the seasonal variation is a major perturbation caused by the onset and subsequent decay of the dust storm that originated in the Noachis Terra region. It is necessary to select intervals of L_s sufficiently broad to insure adequate coverage in longitude but not so broad as to include substantial temporal change in the temperatures. The four intervals chosen are listed in Table 1. These are intended to be representative of conditions near northern fall and spring equinoxes and northern winter solstice. Also included is a time interval near the peak of the Noachis dust storm.

4. RESULTS AND DISCUSSION

Estimates of mean meridional temperature cross sections were made for each of the time intervals indicated in Table 1. Mean temperatures in 2° latitude bins were calculated for each of the standard pressure levels for which temperatures were retrieved. An average of the surface pressures used in the retrievals was also calculated for each bin. Cross sections were then constructed using the mean temperatures for all points in each bin for which the pressure does not exceed the mean surface pressure. The results are presented in Figs. 5a, 6a, 7a and 8a.

The zonal thermal wind field was estimated from the temperature field assuming gradient wind balance in the horizontal and hydrostatic balance in the vertical, resulting in the thermal wind relation (see for example Andrews et al. (1987))

$$\frac{\partial}{\partial z}\left[\left(f + \frac{\bar{u}\tan\theta}{a}\right)\bar{u}\right] = -\frac{R}{ma}\frac{\partial \bar{T}}{\partial \theta} \tag{15}$$

where $\bar{T}$ is the zonal mean temperature, $\bar{u}$ is the zonal mean eastward wind component, θ is latitude, f is the Coriolis parameter, a is the planetary radius, R is the gas constant, and m is the atmospheric mean molecular weight. It is assumed that $\bar{u} = 0$ at the planetary surface, and equation (15) is integrated upward, yielding the baroclinic component of the wind field. Any non-zero surface wind must be added to the result to obtain the total wind speed. Although the calculation of $\bar{u}$ from (15) is simple in principle, care must be taken because of the required numerical differentiation of the temperature with respect to latitude. For this purpose, the temperatures were smoothed in latitude with a 10°–wide window on centers spaced 5°. The resulting zonal thermal wind cross sections are shown in Figs. 5b, 6b, 7b and 8b.

Equinoxes

The mean meridional temperature cross section for the period $L_s = 190-200$ (Fig. 5a) and the related gradient thermal winds (Fig. 5b) show significant hemispheric asymmetry even though it is only a short time after the northern hemisphere autumnal equinox. Temperatures above the 1 mbar level reach a maximum at northern mid latitudes, then decrease rapidly toward the north polar regions where the temperatures are observed to be

$\sim$ 10K cooler than near the south pole. The resulting strong gradient in the north supports a more intense eastward jet in that hemisphere with thermal wind speeds reaching 100 m s^{-1} at the highest levels for which information is available from the present data set. In contrast, in the southern hemisphere, the temperature gradients are weaker, with eastward thermal winds poleward of about 25 S achieving maximum speeds less than half those in the northern hemisphere. Between the equator and 25 S, weak westward thermal winds are observed. Examination of Fig. 5a suggests that the mean meridional temperature cannot be in radiative equilibrium, and is significantly modified by the atmospheric dynamics. The temperature maximum at mid-northern latitudes presumably results from adiabatic warming associated with the descending branch of the mean meridional residual (Hadley) circulation (Andrews et al. 1987); upward motion occurs at low latitudes. The equivalent circulation in the south appears to be significantly weaker.

Fig. 7a shows the mean meridional thermal structure for $L_s = 2 - 4$, just after the northern hemisphere spring equinox. The associated zonal thermal wind field is shown in Fig. 7b. As in the case of the fall equinox, the winds are predominantly eastward in both hemispheres, but there remains some asymmetry. Although the thermal asymmetry is less pronounced than that near the autumnal equinox, and the temperatures near the north and south poles are similar, higher temperatures at northern mid latitudes result in a stronger poleward gradient and stronger thermal winds in the north than in the south.

Results have been published from simulations for several portions of the Martian seasonal cycle using the Ames MGCM (Haberle, et al. 1993) and a Mars adaptation of the Princeton GFDL model (Wilson and Hamilton, 1996). In each case, experiments were run for several different spatially and temporally constant dust optical depths. Haberle et al. present zonal and temporal mean cross sections for the period $L_s = 0 - 23$ and a visible dust optical depth of 0.3. The general magnitudes of the temperatures and thermal winds are comparable to those observed for $L_s = 2 - 4$. The model thermal cross section shows considerable symmetry in the region between approximately 40 S and 40 N, but at higher latitudes, temperatures decrease more rapidly toward the pole in the southern hemisphere than in the north. The wind field is dominated by broad eastward jets in both hemispheres with somewhat higher wind speeds in the south. The observations show

stronger poleward temperature gradients and higher thermal wind speeds in the north. This difference may be due to the fact that the time period over which the model results were averaged is different from that of the observations, and the temperature and wind configurations are changing rapidly. Wilson and Hamilton do not display their equinoctial results, but state that simulations for conditions near $L_s = 180$ produce a circulation that is nearly hemispherically symmetric with broad eastward jets having maxima near 60° latitude. In comparison, the observations for $L_s = 190 - 200$ indicate thermal winds in the northern hemisphere approximately twice as strong as those in the south.

Solstice

The zonal mean meridional temperature cross section for $L_s = 270 - 280$ near northern hemisphere winter solstice is shown in Fig. 6a and the thermal wind field in Fig. 6b. In the northern hemisphere, the eastward jet has become more concentrated in latitude and has intensified, resulting in a strong circumpolar vortex. Maximum thermal wind speeds in excess of 160 m s^{-1} are reached at the upper boundary of the region included in these results. The temperature maximum aloft at high northern latitudes has become stronger relative to the near-equinox conditions, suggesting an intensification of the residual meridional circulation and a resulting increase in adiabatic warming. This warming, combined with the strong radiative cooling of the north polar atmosphere, presumably results in the strong latitude temperature gradients observed in the region centered near 60 N.

In the southern hemisphere, maximum atmospheric temperatures are observed in the south polar region where strong diurnally integrated solar heating is occurring; as a consequence, thermal winds are predominantly westward in this hemisphere. The observed meridional thermal structure appears to deviate strongly from radiative equilibrium, and is consistent with a solstitial cross-equatorial Hadley circulation extending from high southern latitudes to high northern latitudes (Schneider, 1983; Zurek et al., 1992; Haberle et al., 1993; Wilson, 1997).

Haberle et al. (1993) give model results averaged over the period $L_s = 255 - 286$ that can be compared with the TES results for $L_s = 270 - 280$. During the time of the observations, the observed 9-μm dust optical depths were near 0.2 (Smith et al., 1999b);

if the ratio of visible to 9-μm optical depth is assumed to be 2.5 (Martin, 1986), the appropriate visible optical depth would be about 0.5. The observed thermal structure appears to be essentially bracketed by the model results for optical depths of 0.3 and 1.0, but are somewhat closer to the case for an optical depth of 1.0. The general features of the thermal winds derived from the temperature observations agree with those of the model wind field with the exception of a low-level eastward jet centered near 30 S seen in the model. This jet results from the near-angular momentum conserving southward flow of the lower branch of the Hadley circulation (Haberle et al., 1993; Hourdin et al., 1993; Wilson and Hamilton, 1996), and can be regarded as a barotropic component of the flow not accessible to the thermal wind calculation. However, a low-level eastward jet in this latitude region has been inferred from pressure gradients on a constant geopotential surface observed in the radio occultation results (Hinson et al., 1999).

Noachis Dust Storm

Abrupt increases in the 0.3 mbar temperatures at both 30S and 30N can be seen in Fig. 4 at L_s values of 184, 225, and 309. These temperature increases correspond to the onset of regional dust storms in the southern hemisphere. A detailed description of the behavior of the thermal infrared dust opacity as inferred from TES spectra is given by Smith et al. (1999b). The increased temperatures in the south can result from enhanced local heating by the absorption of solar energy by the dust, while the temperature increases in the north presumably are produced by a dynamic response. Because of the spatial and temporal distribution of the TES data set at this time, it is difficult to precisely quantify any time lag in the northern hemisphere temperature increase relative to that in the south, but if such a lag exists, it cannot be greater than 2–3 sols.

The large temperature increases seen in Fig. 4 near $L_s = 225$ correspond to the Noachis Terra dust storm. This storm was near its maximum intensity during the period $L_s = 225 - 233$ (Smith et al. 1999b), and this is the final period to be considered here. Although regional, this storm had a profound effect on the global thermal structure. The meridional temperature and thermal wind cross sections are shown in Figs. 8a and 8b respectively. A temperature maximum is seen at low levels in the southern hemisphere,

centered near 30 S where the atmospheric dust loading is greatest. In the northern hemisphere, a strong temperature maximum is observed near 60 N, presumably due to a rapid intensification of the cross-equatorial meridional circulation and accompanying increased adiabatic warming in the downward branch. An intense horizontal temperature gradient lies poleward of this maximum. This polar front shows a strong poleward tilt with increasing height, and the core of a strong polar vortex penetrates to 60 N near the 0.3 mbar level.

Similar rapid enhancement of temperatures at high northern latitudes was observed in the Viking IRTM 15–μm channel data during global dust storm conditions (Martin and Kieffer, 1979; Jakosky and Martin, 1987). A number of global dust storm numerical simulations have been published (Murphy et al., 1993; Murphy et al., 1995; Wilson, 1997) as well as numerical experiments with fixed, large dust opacities. The Noachis storm was regional, never achieving global status, and occurred approximately mid way between equinox and solstice, while the simulations have been directed primarily at near-global atmospheric dust loading and solstitial seasonal conditions. Nevertheless, the observed thermal structure exhibits behavior qualitatively similar to some of the simulations. For example, Wilson's (1997) results show high temperatures aloft poleward of 60 N and an intense circumpolar jet core at very high latitudes. However, in the southern hemisphere, the TES temperatures do not show the monotonic increase toward the south pole, but reach a maximum near 60 S and then decrease toward the pole. This results in an eastward thermal wind at high southern latitudes not seen in the model. This may be a consequence of the earlier occurrence in the season of the Noachis storm, prior to the establishment of a strong pole-to-pole meridional circulation. In addition, a decrease in the atmospheric dust toward the south pole could also contribute to the lower temperatures there.

Waves

The temperature standard deviations associated with the mean thermal structure for each of the four time intervals considered are shown in the form of meridional cross sections in Figs. 9–12. Contributions to these standard deviations include propagation of random errors into the retrievals, strong temperature latitude gradients within the averaging bins,

seasonal evolution of the temperature field during the time intervals over which the averages are taken, and the combined effects of the various atmospheric wave modes that may be present. The contribution due to the total random errors in the individual retrievals away from the surface is of the order of 1–2 K, the use of sliding averaging bins minimizing the effects of temperature gradients, and the time intervals analyzed were chosen to minimize the possible secular changes occurring during each interval. From these considerations, standard deviations in excess of 4–5 K can be regarded as indicators of significant wave activity. Stationary planetary waves, tidal modes, and traveling disturbances can all contribute to the observed temperature standard deviations. Given the spatial and temporal sampling of the data obtained by TES, isolation and characterization of individual wave modes is challenging. An investigation of the possible wave modes present in the TES temperature fields has been carried out by Banfield et al. (1999).

We now briefly considered some possible implications of the temperature standard deviations. The cross section of standard deviations for $L_s = 190 - 200$ (Fig. 9) shows no concentrated regions of temperature fluctuations with the possible exceptions of low atmospheric levels at mid southern latitudes and near 70 N. In contrast, the results shown in Fig. 10 for the time interval near northern winter solstice ($L_s = 270 - 280$) suggests the presence of strong wave activity at low and mid latitudes in the southern hemisphere and in a confined latitude range centered near 60 N. In the south, large standard deviations are observed between the surface and approximately the 1 mbar level; these are especially intense just south of the equator and may be related to wave activity at these latitudes associated with the Tharsis ridge. At 60 N, the maximum standard deviation occurs just below the 1 mbar level, and the temperature fluctuations are highly correlated with the wind field (Fig. 6b), suggesting ducting of waves into the polar vortex region. It is interesting to note that in the northern hemisphere between the equator and 50 N, the temperature field is extremely quiescent. For the time interval near northern hemisphere spring equinox ($L_s = 2 - 4$) shown in Fig. 11, the standard deviations are similar to those near the fall equinox with relatively weak temperature fluctuations. For the period during the Noachis dust storm ($L_s = 225 - 233$) shown in Fig. 12, there appears to be significant wave activity at almost all latitudes with the possible exception of the region between the

equator and about 40 N. There are large standard deviations associated with the polar vortex, with maximum values near the 0.3 mbar level at 70 N, again suggesting strong wave activity in this region.

5. SUMMARY

A temperature inversion algorithm has been applied to virtually the entire data base of TES thermal emission spectra acquired during the period from mid-September 1997 through September 1998. Selected samples of the resulting temperature profiles have been used to produce cross sections of temperature and thermal winds that document the seasonal progression over half of a Martian year, and the influence of a regional dust storm on the atmospheric structure.

Results from time intervals near both northern hemisphere fall and spring equinoxes show some hemispheric asymmetry was present with stronger high latitude temperature gradients, and consequently, stronger thermal winds in the northern hemisphere in both cases. Wave activity, as measured by temperature variances, appears to have been relatively weak throughout most of the atmosphere at these times. Near solstice, the results were found to be highly asymmetric between hemispheres, with temperatures monotonically increasing at all levels toward the south pole resulting in westward thermal winds throughout the southern hemisphere. A strong, deep polar front was observed at high northern latitudes, associated with the polar vortex. Observed temperature variance suggests that ducting of waves into the vortex was occurring.

The good general agreement of the observations with the results from general circulation modeling experiments is encouraging although some differences in detail exist. Somewhat better agreement is obtained with models incorporating larger dust optical depths than those indicated by the TES dust retrievals (Smith et al., 1999). These differences may be minimized in future model experiments that more nearly duplicate the conditions existing during the TES measurements.

Even though the TES data analyzed here were taken prior to the beginning of the MGS mapping mission, they have provided the most nearly complete description of atmospheric thermal structure over half of a Martian seasonal cycle yet acquired. It is anticipated

that this data base will be greatly extended and enhanced with retrievals from regularly sampled measurements of both limb and nadir spectra to be obtained during the mapping mission.

ACKNOWLEDGMENTS

The authors are grateful to Emily Greene, Karen Horrocks, Carolyn Martin, Richard Thompson, and Eric Winter for providing software development and data handling expertise at Goddard Space Flight Center. The contributions of Kelly Bender, Noel Gorelick, and Greg Mehall at Arizona State University were essential to the success of this work. Todd Clancy and Peter Gierasch provided helpful comments on an earlier version of the manuscript. The work was supported in part by the Mars Global Surveyor Project and the Mars Exploration Directorate Office of Strategy and Science of the Jet Propulsion Laboratory.

REFERENCES

Andrews, D. G., J. R. Holton, and C. B. Leovy, *Middle Atmosphere Dynamics*, Academic Press, New York, 1987.

Bandfield, J. L., P. R. Christensen, and M. D. Smith, Spectral dataset factor analysis and endmember recovery: Application to analysis of Martian atmospheric particulates, submitted to *J. Geophys. Res.*, 1999.

Banfield, D., B. J. Conrath, J. C. Pearl, M. D. Smith, and P. R. Christensen, Thermal tides and stationary waves on Mars as revealed by MGS TES, *J. Geophys. Res.*, this issue, 1999b.

Christensen, P. R., D. L. Anderson, S. C. Chase, R. N. Clark, H. H. Kieffer, M. C. Malin, J. C. Pearl, J. Carpenter, N. Bandiera, F. G. Brown, and S. Silverman, Thermal Emission Spectrometer Experiment: Mars Observer Mission, *J. Geophys. Res., 97*, 7719–7734, 1992.

Christensen, P. R., D. L. Anderson, S. C. Chase, R. T. Clancy, R. N. Clark, B. J. Conrath, H. H. Kieffer, R. O. Kuzmin, M. C. Malin, J. C. Pearl, T. L. Roush, and M. D. Smith, Results from the Mars Global Surveyor Thermal Emission Spectrometer, *Science, 179*, 1692–1698, 1998.

Conrath, B., R. Curran, R. Hanel, V. Kunde, W. Maguire, J. Pearl, J. Pirraglia, J. Welker, and R. Burke, Atmospheric and surface properties of Mars obtained by infrared spectroscopy on Mariner 9, *J.Geophys. Res., 78*, 4267–4278, 1973.

Conrath, B. J., Thermal structure of the Martian atmosphere during the dissipation of the dust storm of 1971, *Icarus, 24*, 36–46, 1975.

Conrath, B. J., Influence of planetary-scale topography on the diurnal thermal tide during the 1971 Martian dust storm, *J. Atmos. Sci., 33*, 2430–2439, 1976.

Conrath, B. J., Planetary scale wave structure in the Martian atmosphere, *Icarus, 48*, 246–255, 1981.

Conrath, B. J., P. J. Gierasch, and E. A. Ustinov, Thermal structure and para hydrogen fraction on the outer planets from Voyager IRIS measurements, *Icarus, 135*, 501–517, 1998.

Craig, I. J. D., and J. C. Brown, *Inverse Problems in Astronomy*, Adam Hilger, Boston, 1986.

Goody, R., R. West, L. Chen, and D. Crisp, The correlated-k method for radiation calculations in nonhomogeneous atmospheres, *JQSRT*, 539-550, 1989.

Haberle, R. M., J. B. Pollack, J. R. Barnes, R. W. Zurek, C. B. Leovy, J. R. Murphy, H. Lee, and J. Schaeffer, Mars atmospheric dynamics as simulated by the NASA Ames general circulation model 1. The zonal-mean circulation, *J. Geophys. Res., 98*, 3093–3123, 1993.

Hanel, R. A., B. Conrath, W. Hovis, V. Kunde, P. Lowman, W. Maguire, J. Pearl, J. Pirraglia, C. Prabhakara, B. Schlachman, G. Levin, G. Straat, and T. Burke, Investigation of the Martian environment by infrared spectroscopy on Mariner 9, *Icarus, 17*, 423–442, 1972.

Hinson, D. P., F. M. Flasar, R. A. Simpson, J. D. Twicken, and G. L. Tyler, Initial results from radio occultation measurements with Mars Global Surveyor, *J. Geophys. Res.*, this issue, 1999b.

Hourdin, F., P. L. Van, F. Forget, and O. Talagrand, Meteorological variability and the annual surface pressure cycle on Mars, *J. Atmos. Sci., 50*, 3625–3640, 1993.

Jakosky, B. M., and R. Z. Martin, Mars: North-polar atmospheric warming during dust storms, *icarus, 72*, 528-534, 1987.

Martin, T. Z., Mean thermal and albedo behavior of the Mars surface and atmosphere over a Martian year. *Icarus, 45*, 427–446, 1981.

Martin, T. Z., and H. H. Kieffer, Thermal infrared properties of the Martian atmosphere. 2. The 15 μm band measurements. *J. Geophys. Res., 84*, 2843–2852, 1979.

Martin, T. Z., Thermal infrared opacity of the Mars atmosphere, *Icarus, 66*, 2–21, 1986.

Murphy, J. R., R. M. Haberle, O. B. Toon, and J. B. Pollack, Martian global dust storms; Zonally symmetric numerical simulations including size–dependent particle transport, *J. Geophys. Res., 98*, 3197–3220, 1993.

Murphy, J. R., J. B. Pollack, R. M. Haberle, C. B. Leovy, O. B. Toon, and J. Schaefer, Three dimensional numerical simulation of Martian global dust storms, *J. Geophys. Res., 100*, 26357–26376, 1995.

Schneider, E. K., Martian great dust storms: Interpretive axially symmetric models, *Icarus*, *55*, 302–331, 1983.

Smith, M. D., J. L. Bandfield, and P. R. Christensen, Separation of atmospheeric and surface spectral features in Mars Global Surveyor Thermal Emission Spectrometer (RES) spectra, submitted to *J. Geophys. Res.*, 1999b.

Smith, M. D., B. J. Conrath, J. C. Pearl, and P. R. Christensen, Mars Global Surveyor thermal emission spectrometer (TES) observations of dust opacity during aerobraking and science phasing, *J. Geophys. Res.*, this issue, 1999b.

Tillman, J. E., N. C. Johnson, P. Guttorp, and D. B. Percival, The Martian annual atmospheric pressure cycle – Years without great dust storms, *J. Geophys. Res.*, *98*, 10,963–10,971, 1993.

U.S. Geological Survey, *Mars Digital Terrain Models CD Volume 7: Global Topography*, USA_NASA_PDS_VO_2007, Version 2, 1993.

Wilson, J. R., A general circulation model simulation of the Martian polar warming, *Geophys. Res. Letters*, *24*, 123–126, 1997.

Wilson, J. R., and K. Hamilton, Comprehensive model simulation of thermal tides in the Martian atmosphere, *J. Atmos. Sci.*, *53*, 1290–1326, 1996.

Zurek, R. W., J. R. Barnes, R. M. Haberle, J. B. Pollack, J. E. Tillman, and C. B. Leovy, Dynamics of the atmosphere of Mars, in *Mars*, H. H. Kieffer, B. M. Jakosky, C. W. Snyder, and M. S. Matthews, editors, U. of Arizona Press, Tucson, 1992.

FIGURE CAPTIONS

Figure 1. Contribution functions (functional derivatives of radiance with respect to temperature) for the wavenumbers used in the temperature retrievals. These functions were calculated using equation (10) in the text, and are for the nominal TES 10 cm^{-1} resolution. Units for the contribution functions are W cm^{-2} $ster^{-1}/cm^{-1}$/kelvin.

Figure 2. Temperature profile retrievals from synthetic data; (a) model representative of a daytime profile with warm surface, and (b) model with strong inversion in the lower atmosphere and a cool surface. The temperature retrievals are compared with the true model profiles and the initial profiles in the left hand panels. In the right hand panels, profiles of the rms error in the retrievals are plotted. The rms error represents the precision of the retrieval in the presence of assumed random errors as discussed in the text. Errors due to surface pressure uncertainties and other systematic errors are not included.

Figure 3. Error covariance matrix for a temperature profile retrieval as defined by eq. (9) of the text. The elements of this symmetric matrix characterize the correlation between atmospheric levels of the temperature retrieval errors due to propagation of instrument noise. The units are $kelvin^2$.

Figure 4. Trends in retrieved temperatures at 0.3 mbar for 30 N (upper panel) and 30 S (lower panel). Temperature is plotted as a function of the seasonal parameter L_s (aerocentric longitude of the sun). The data extend over a period beginning shortly after northern hemisphere fall ($L_s = 180$) through northern winter and into northern spring ($L_s = 360$). The rapid increases in temperature in both hemispheres near $L_s = 225$ result from the onset of the Noachis regional dust storm and are correlated with the sudden increase in dust opacities observed in the southern hemisphere (Smith et al., 1999). The temperature increases seen near $L_s = 310$ correlate with a smaller regional dust storm.

Figure 5. Mean meridional cross sections of (a) retrieved temperatures and (b) gradient thermal winds for the period $L_s = 190 - 200$ near northern hemisphere fall equinox. The temperatures are in kelvins and the wind speeds are expressed in m s^{-1}.

Eastward thermal winds are positive. The mean surface pressures for this data set are indicated at the lower boundary of the coutoured regions.

Figure 6. Same as Figure 5 except for $L_s = 270 - 280$ near northern winter solstice.

Figure 7. Same as Figure 5 except for $L_s = 2 - 4$ near northern spring equinox.

Figure 8. Same as Figure 5 except for $L_s = 225 - 233$ during the Noachis dust storm.

Figure 9. Cross section of rms temperature deviations for $L_s = 190 - 200$. The deviations are expressed in kelvins. Values greater than 2–4 K are probably related to atmospheric wave activity.

Figure 10. Same as Figure 9 except for $L_s = 270 - 280$.

Figure 11. Same as Figure 9 except for $L_s = 2 - 4$.

Figure 12. Same as Figure 9 except for $L_s = 225 - 233$ during the Noachis dust storm.

TABLE 1. Selected Time Intervals for Mean Meridional Cross Sections

L_s	Number of Retrievals	Comments
190–200	67,776	Near N. Hemisphere Fall Equinox
270–280	44,502	N. Hemisphere Winter Solstice
2–4	121,636	N. Hemisphere Spring Equinox
225–233	64,251	Noachis Dust Storm

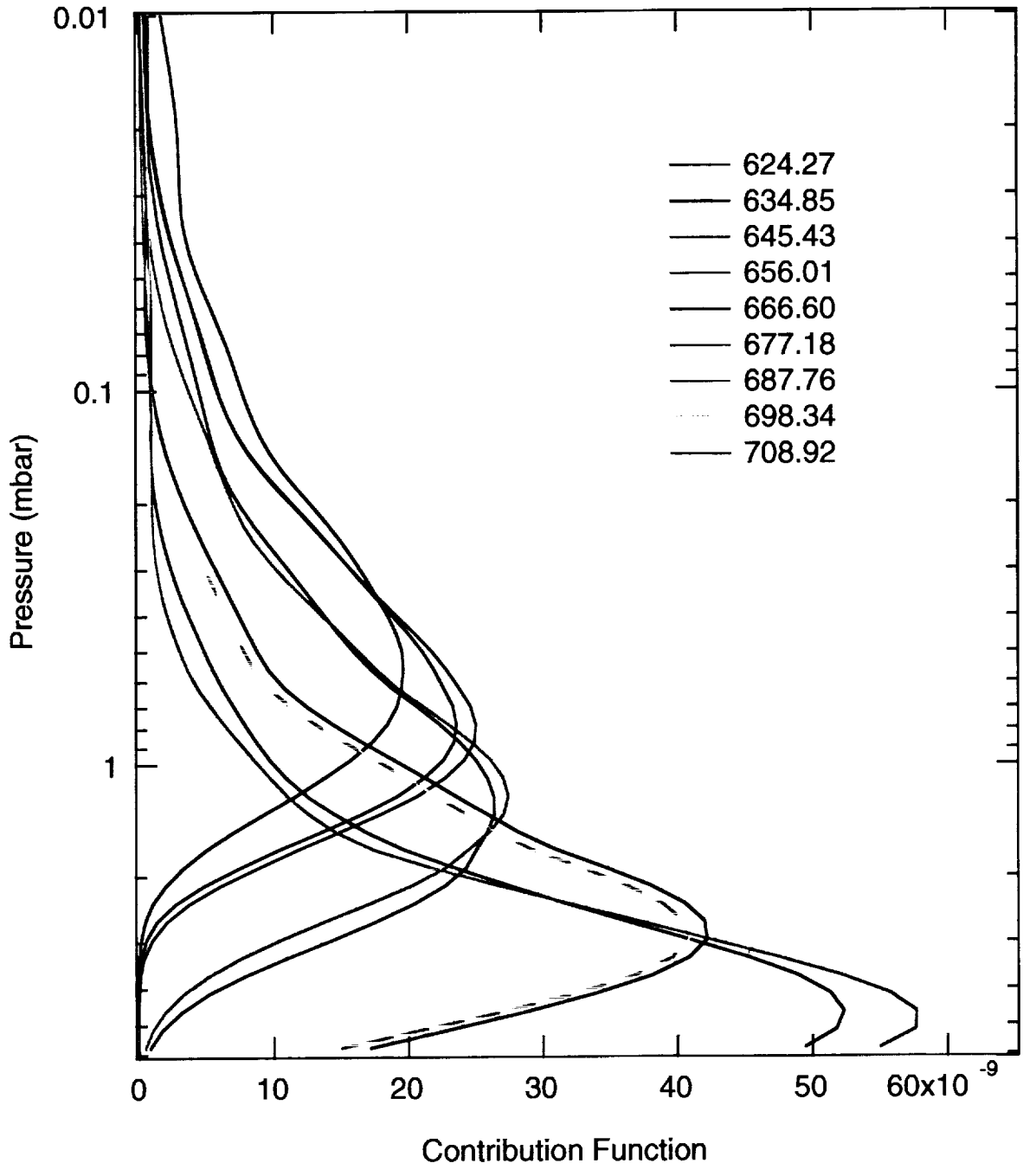
0.01
0.1
1
Pressure (mbar)
624.27
634.85
645.43
656.01
666.60
677.18
687.76
698.34
708.92
0
10
20
30
40
50
60x10 -9
Contribution Function

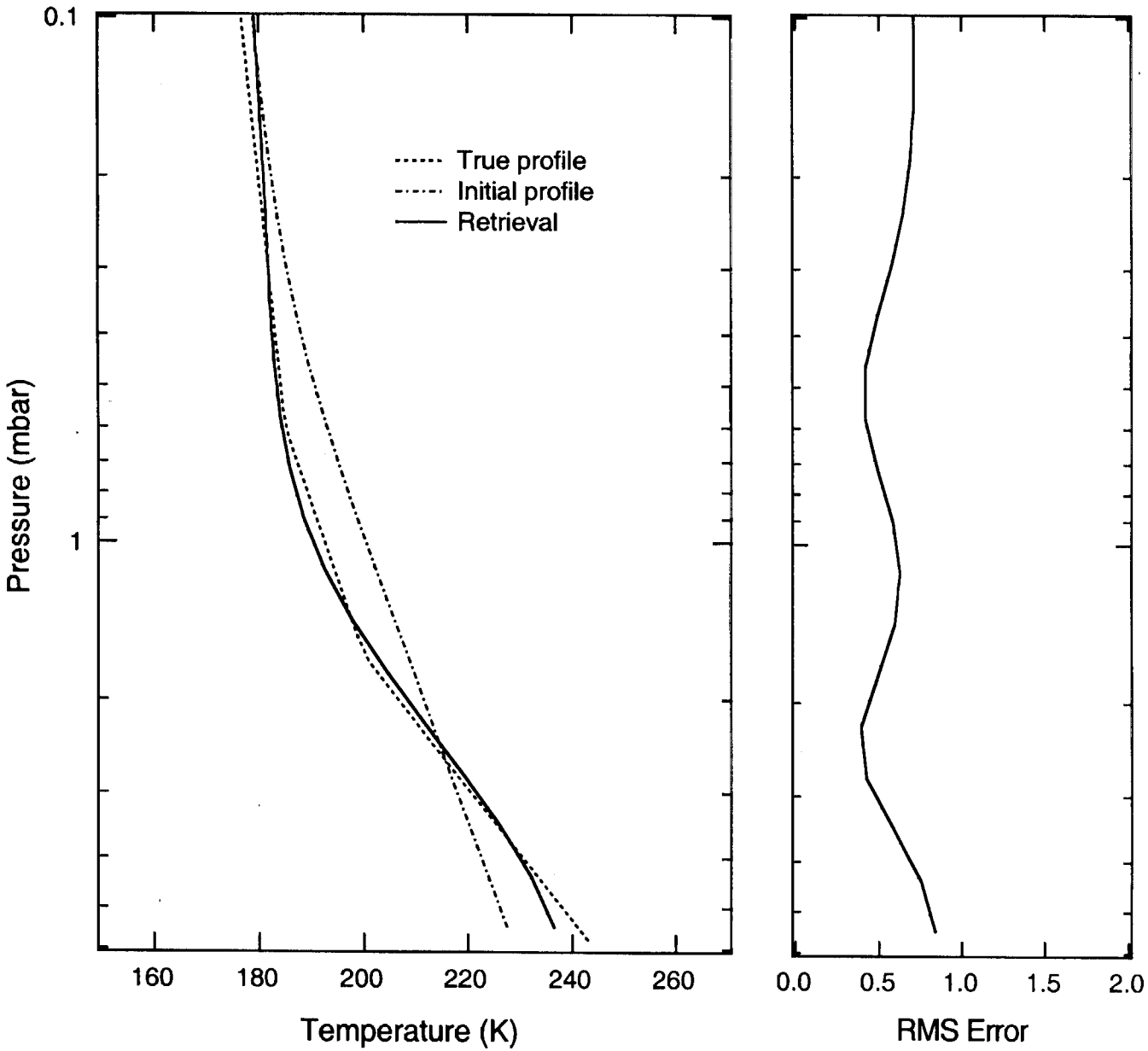
0.1
1
Pressure (mbar)
True profile
Initial profile
Retrieval
160
180
200
220
240
260
Temperature (K)
0.0
0.5
1.0
1.5
2.0
RMS Error

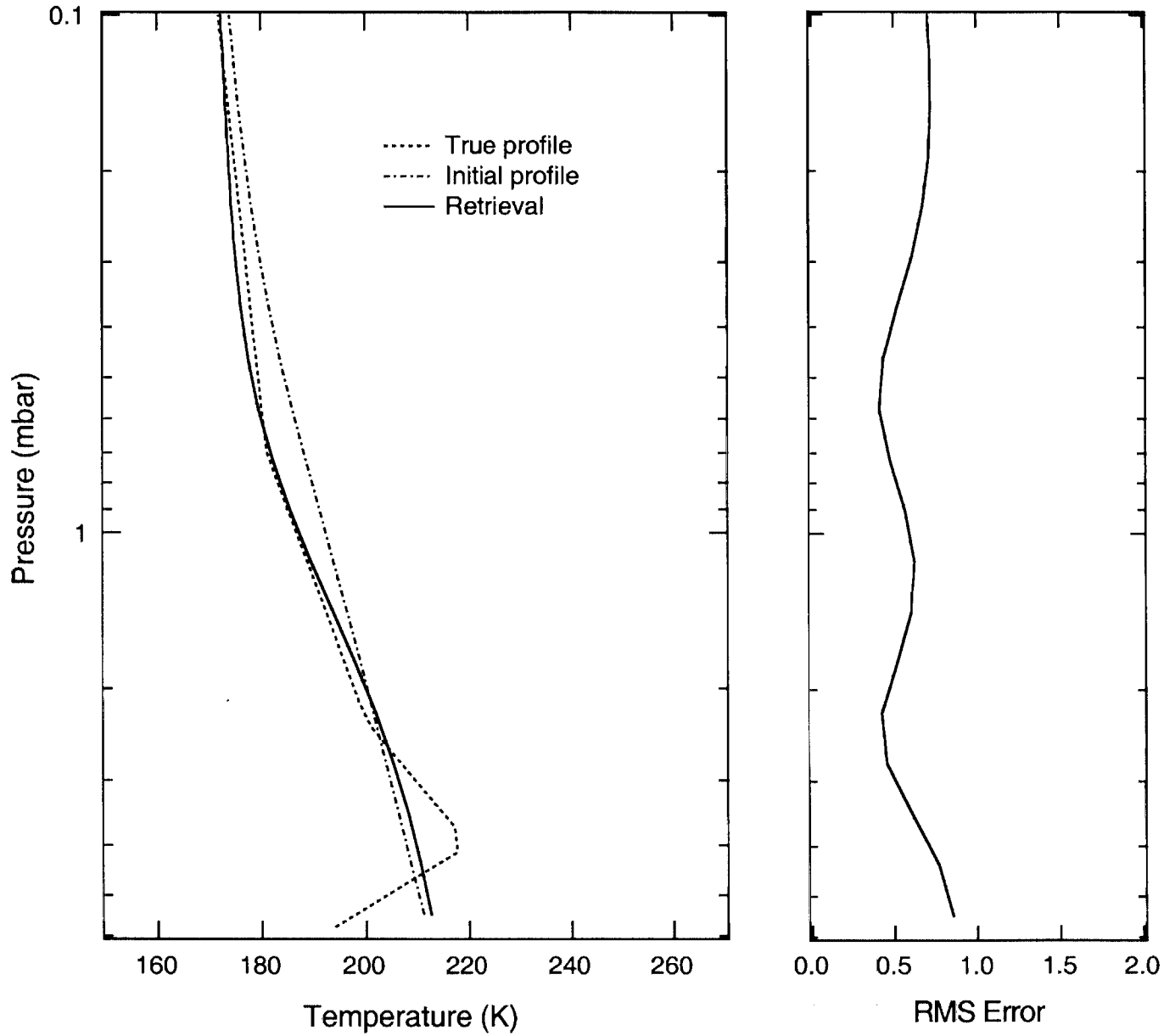
0.1
1
Pressure (mbar)
True profile
Initial profile
Retrieval
160
180
200
220
240
260
Temperature (K)
0.0
0.5
1.0
1.5
2.0
RMS Error

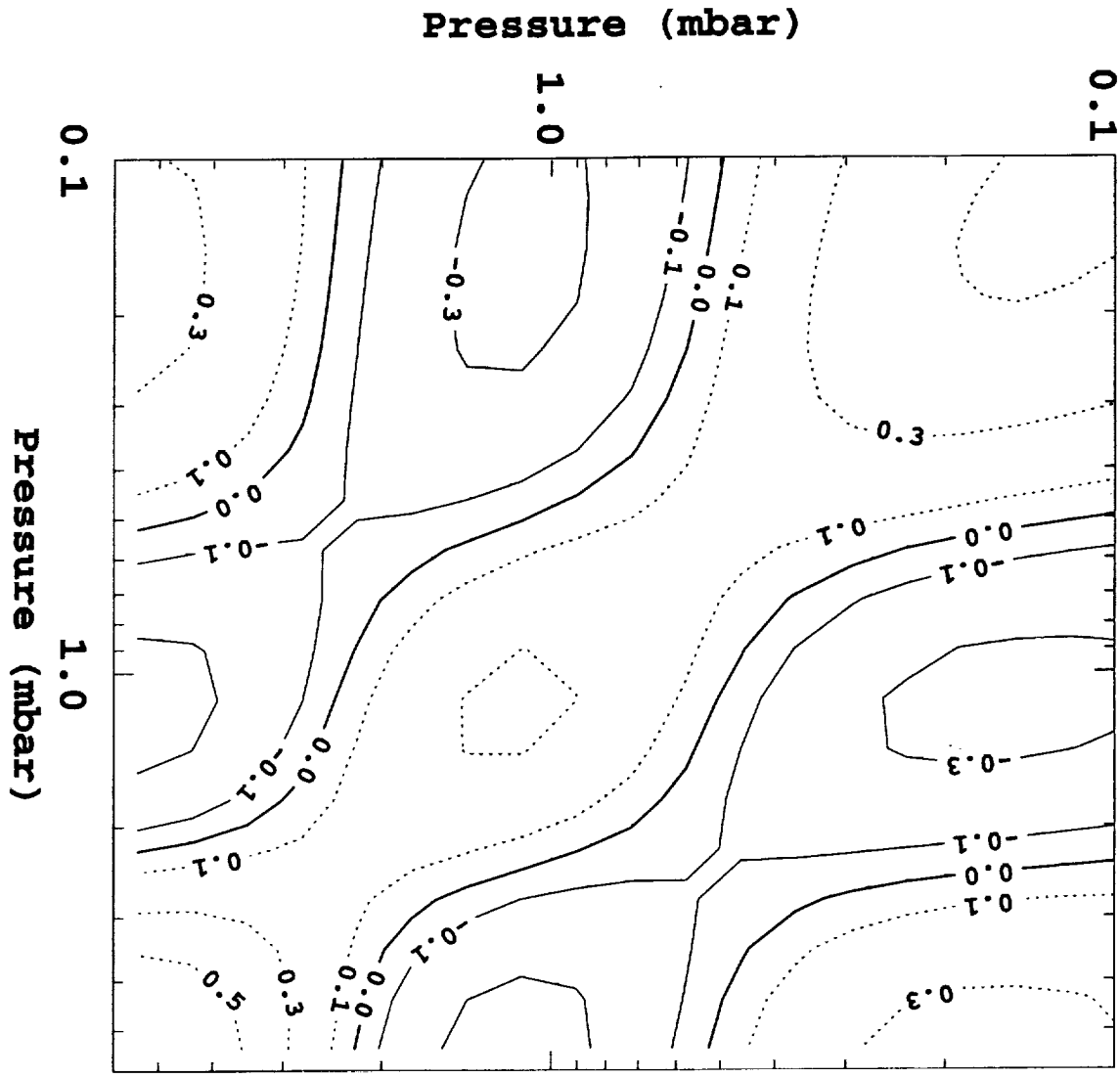
Pressure (mbar)
0.1
1.0
0.1
1.0
Pressure (mbar)
0.3
0.1
0.0
-0.1
-0.3
0.1
0.0
-0.1
0.3
0.1
0.0
-0.1
-0.3
0.0
-0.1
0.1
0.5
0.3
0.1
0.0
-0.1
0.1
0.0
-0.1
0.3

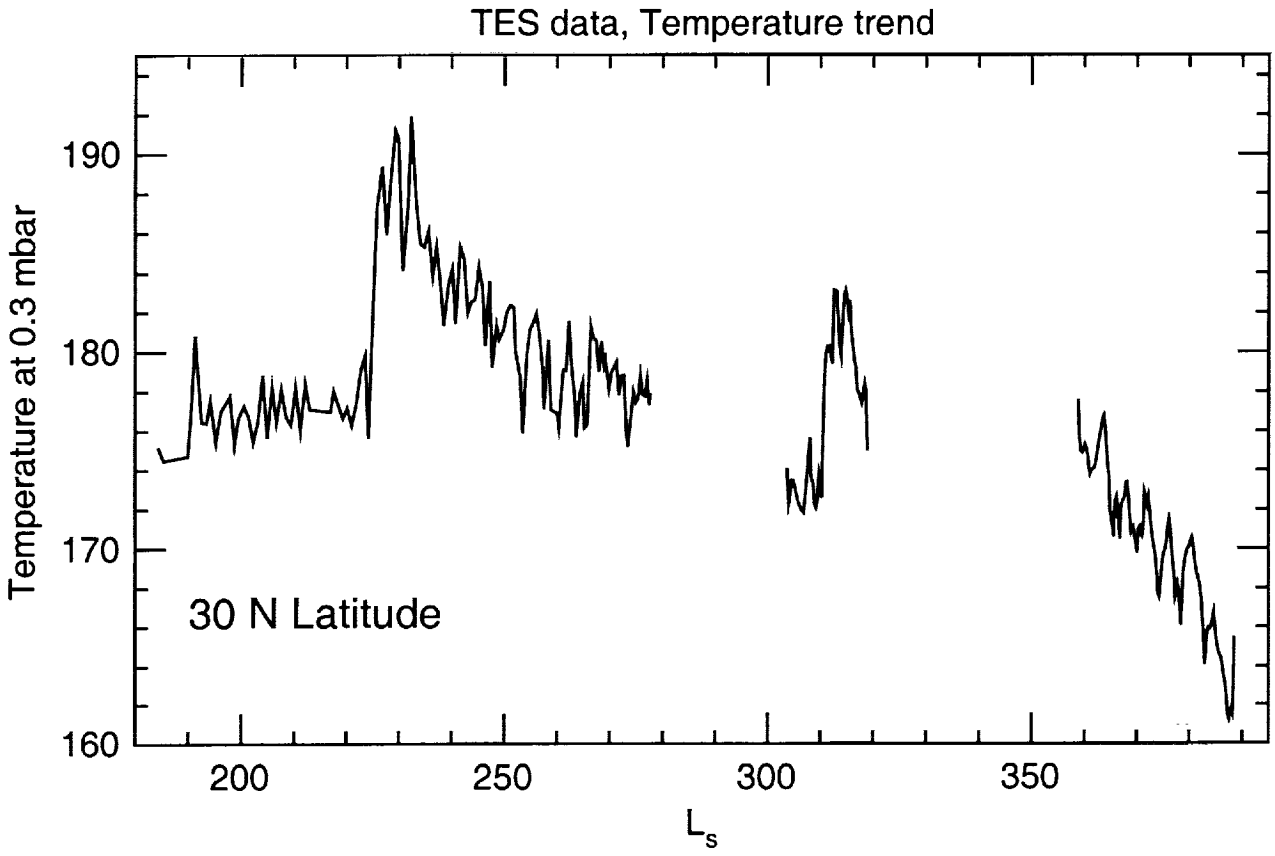
TES data, Temperature trend
Temperature at 0.3 mbar
190
180
170
160
30 N Latitude
200
250
300
350
L_s

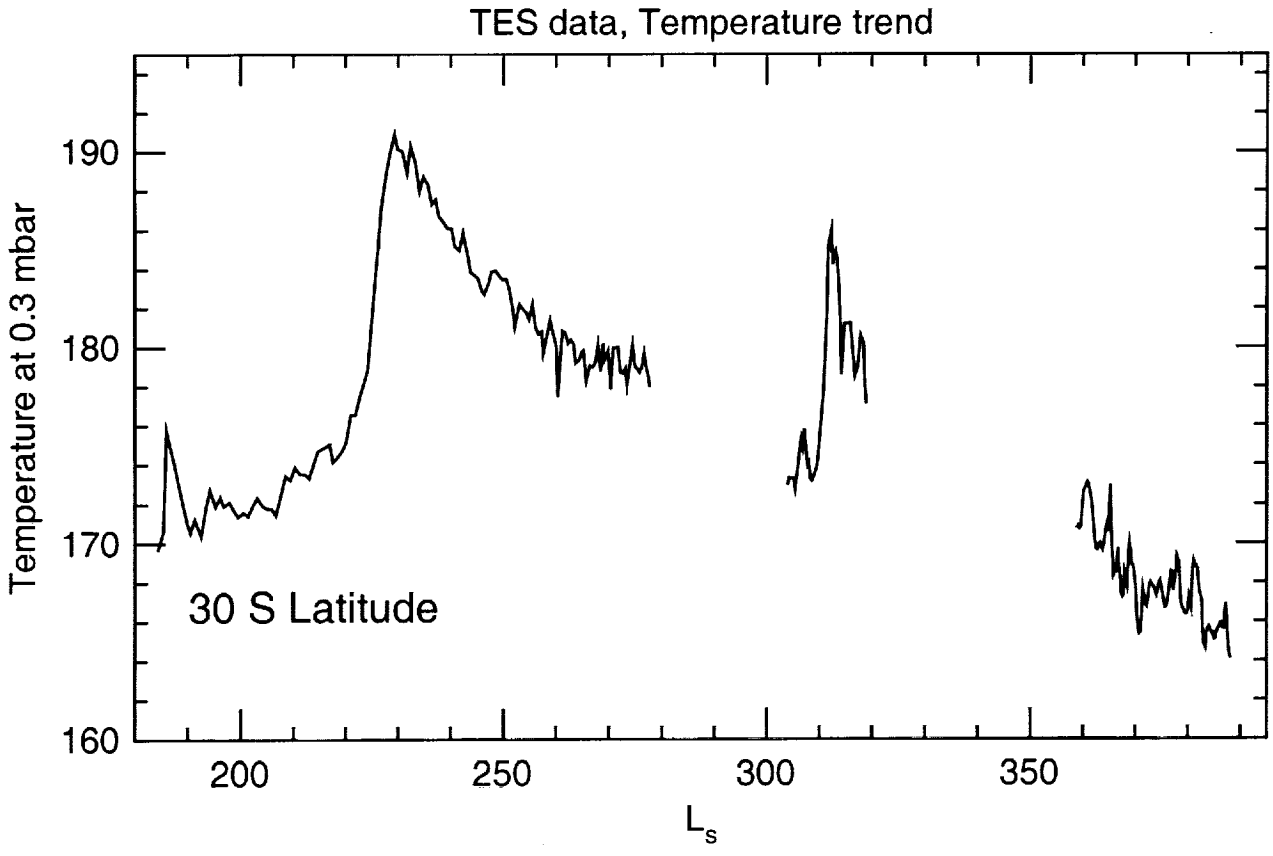
TES data, Temperature trend
Temperature at 0.3 mbar
190
180
170
160
30 S Latitude
200
250
300
350
L_s

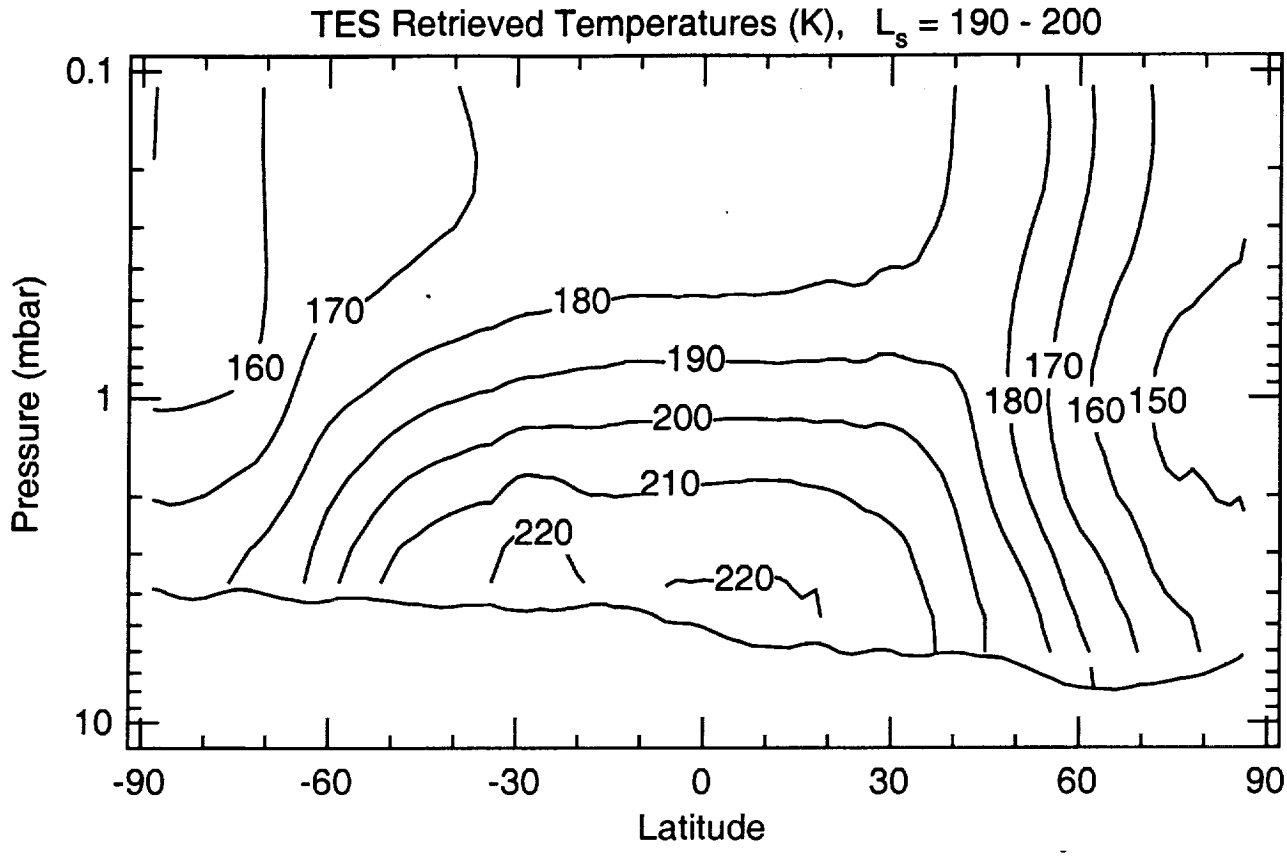
TES Retrieved Temperatures (K), L_s = 190 - 200
Pressure (mbar)
0.1
1
10
160
170
180
190
200
210
220
220
170
180
160
150
-90
-60
-30
0
30
60
90
Latitude

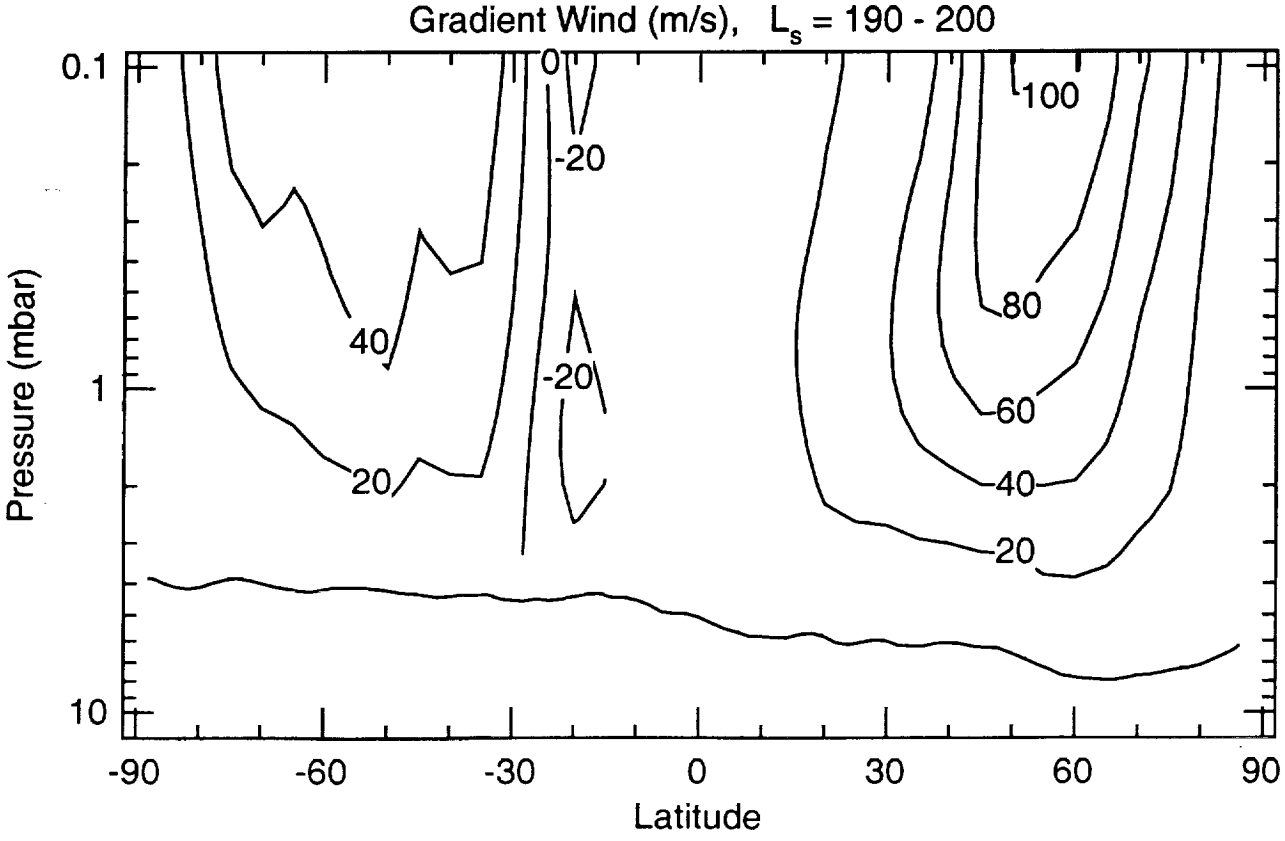
Gradient Wind (m/s), L_s = 190 - 200
Pressure (mbar)
0.1
1
10
0
-20
-20
40
20
100
80
60
40
20
-90
-60
-30
0
30
60
90
Latitude

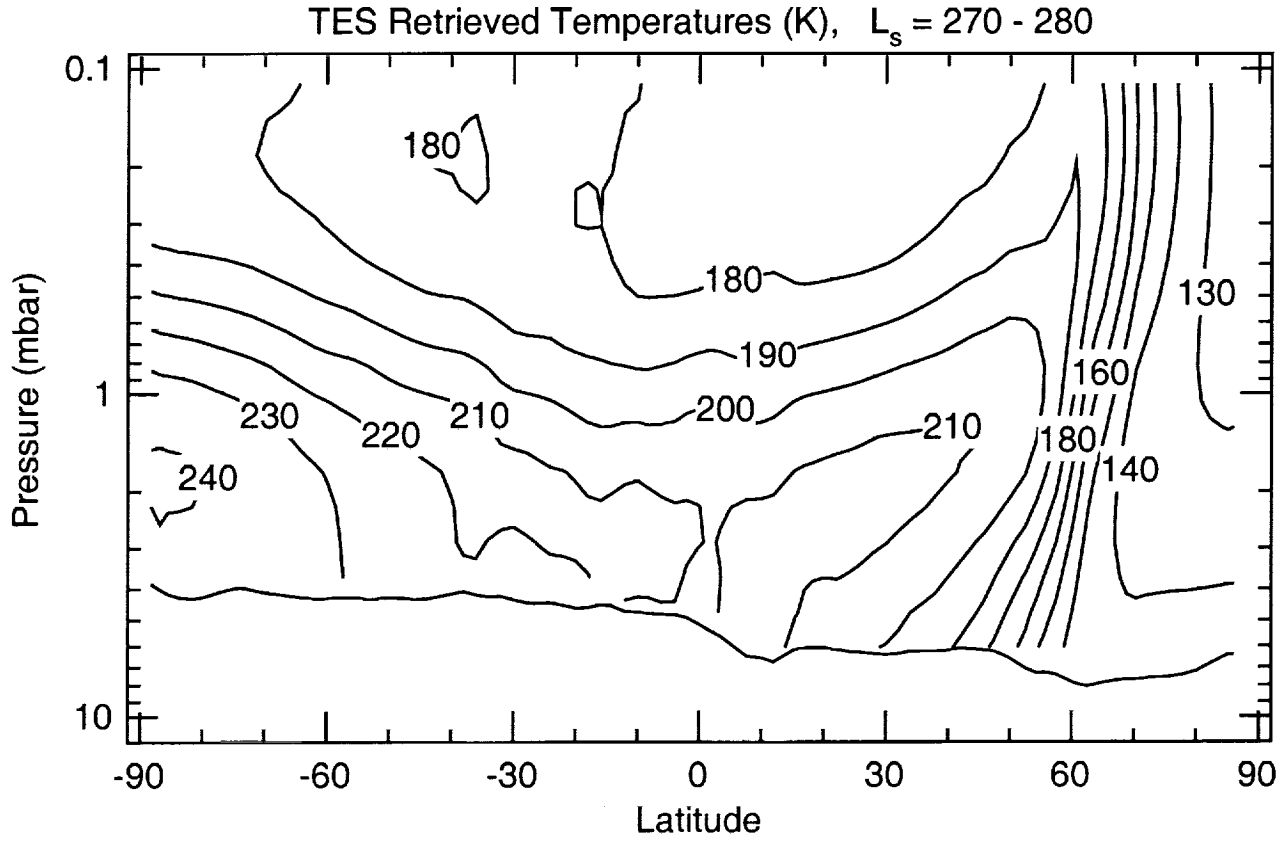
TES Retrieved Temperatures (K), L_s = 270 - 280
Pressure (mbar)
0.1
1
10
180
180
190
200
210
210
220
230
240
130
160
180
140
-90
-60
-30
0
30
60
90
Latitude

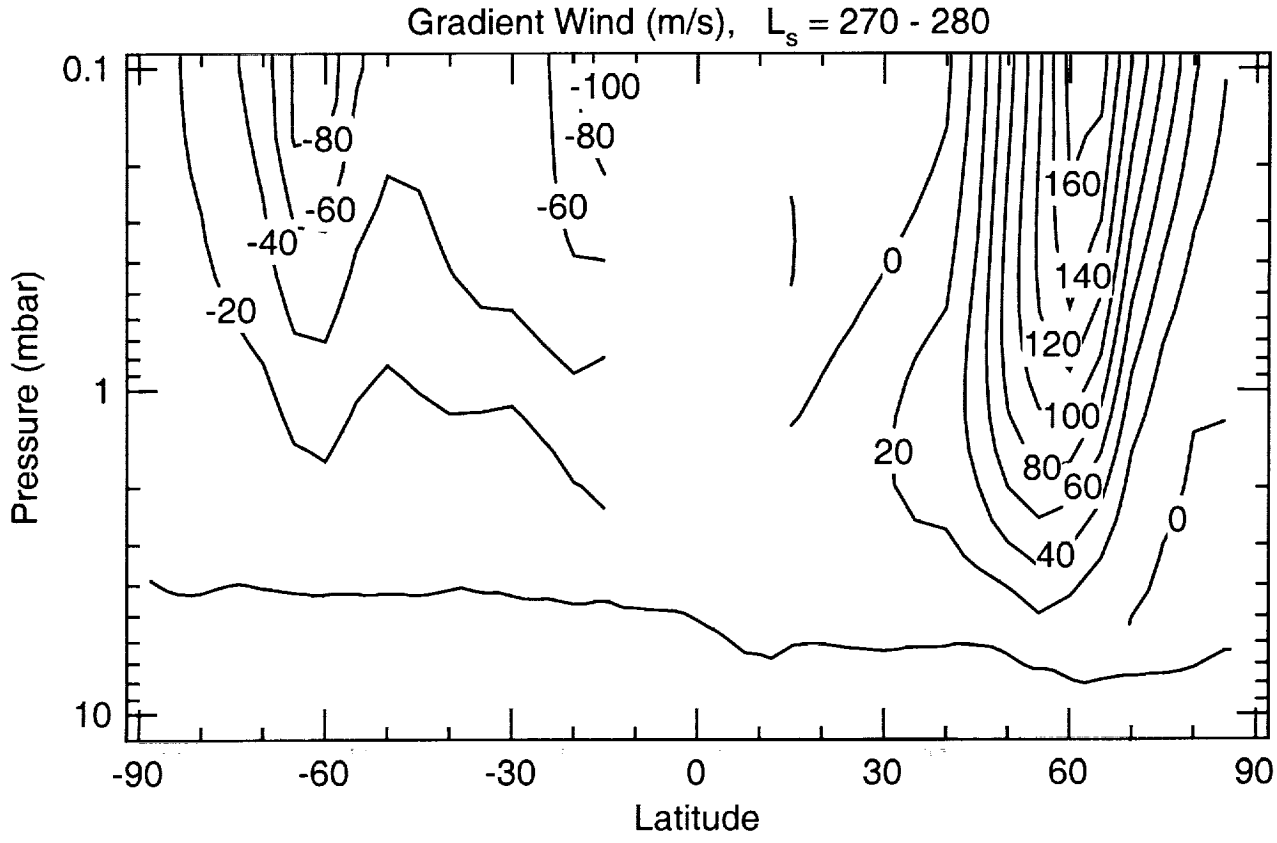
Gradient Wind (m/s), L_s = 270 - 280
Pressure (mbar)
0.1
1
10
-100
-80
-80
-60
-60
-40
-20
0
160
140
120
100
80
60
40
20
0
-90
-60
-30
0
30
60
90
Latitude

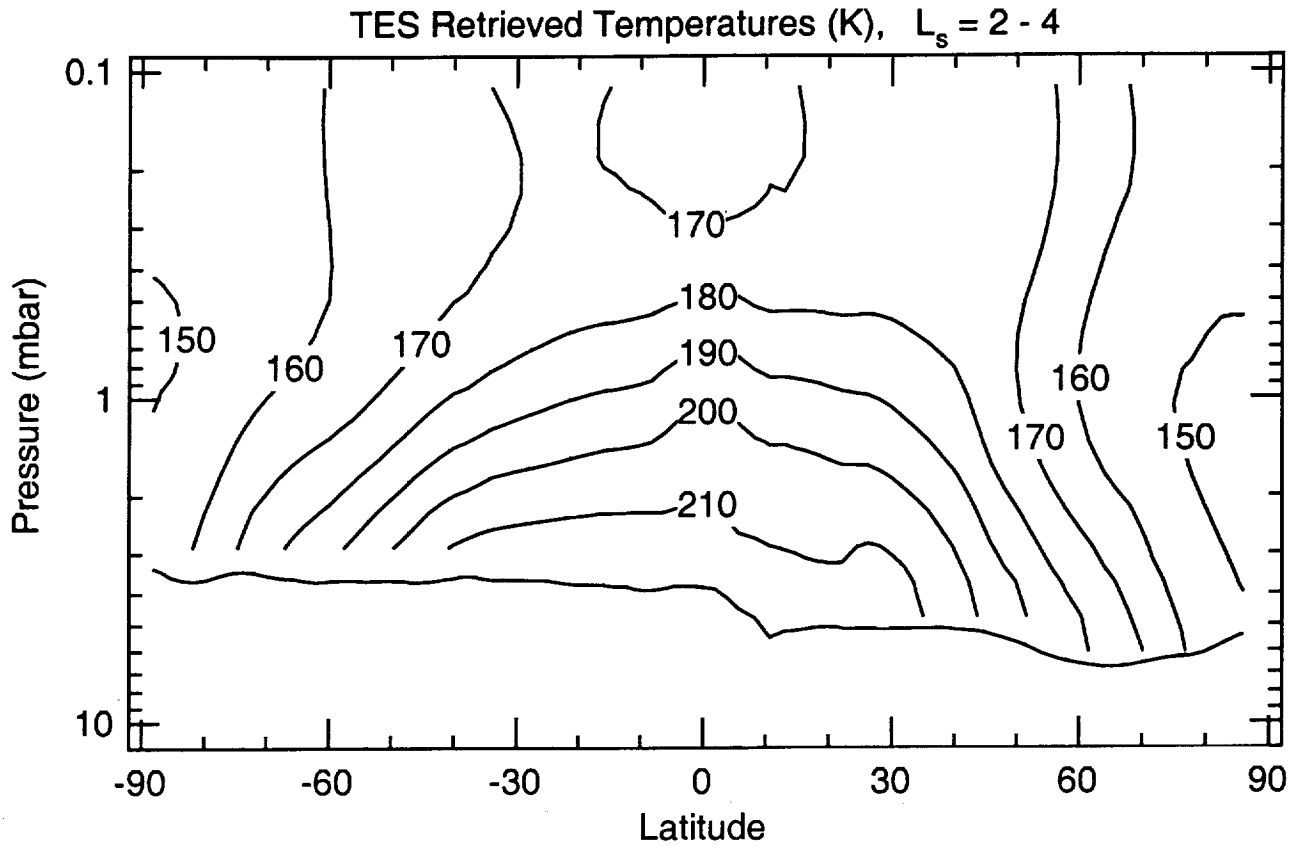
TES Retrieved Temperatures (K), L_s = 2 - 4
Pressure (mbar)
0.1
1
10
150
160
170
180
190
200
210
-90
-60
-30
0
30
60
90
Latitude

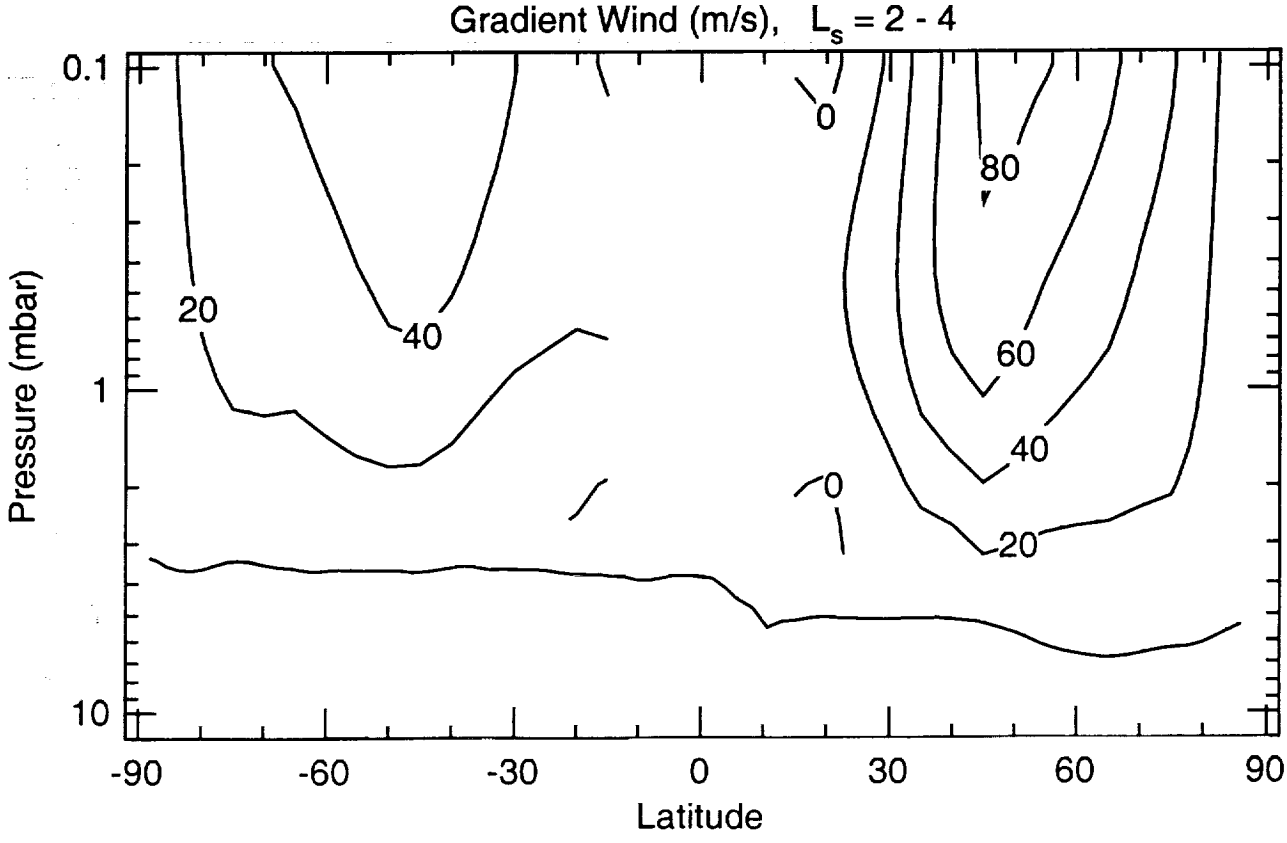
Gradient Wind (m/s), L_s = 2 - 4
Pressure (mbar)
0.1
1
10
20
40
0
80
60
40
0
20
-90
-60
-30
0
30
60
90
Latitude

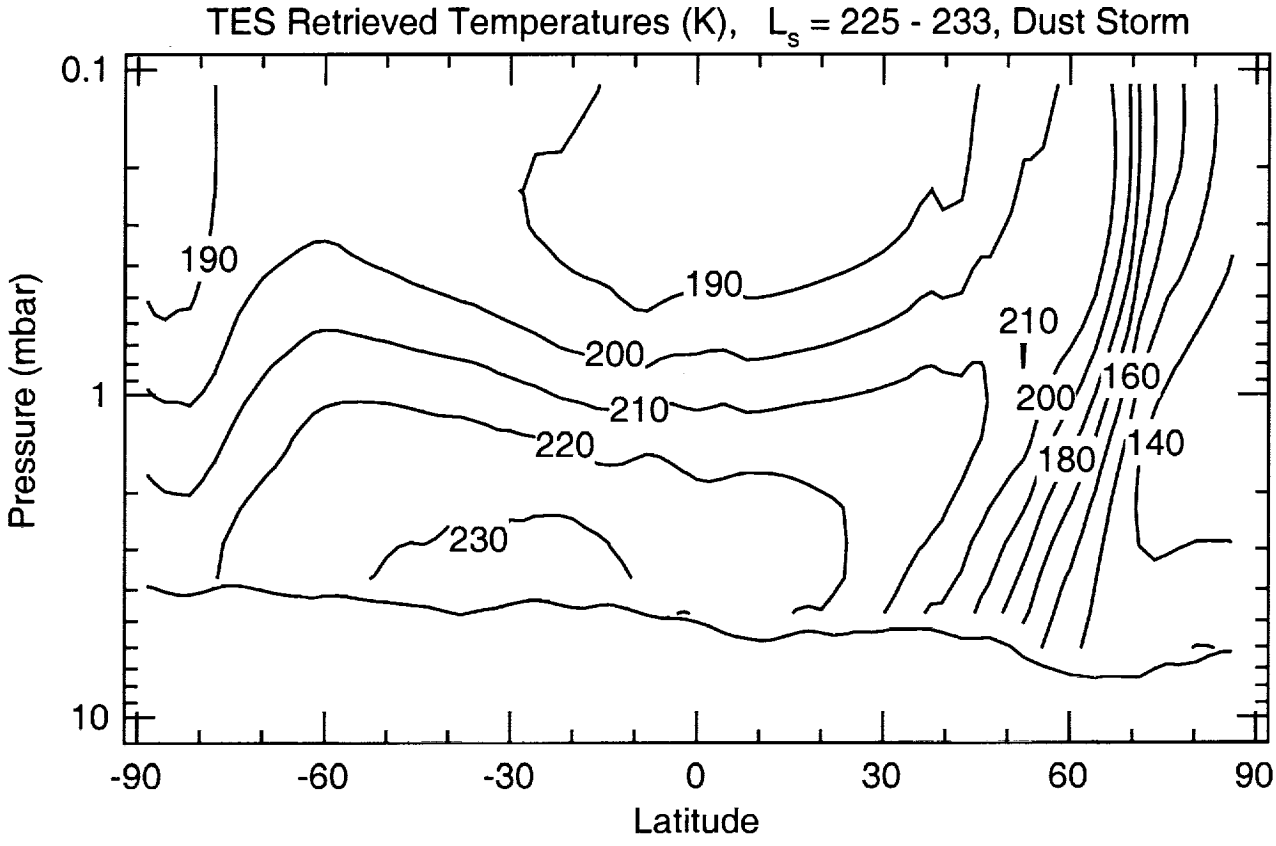
TES Retrieved Temperatures (K), L_s = 225 - 233, Dust Storm
Pressure (mbar)
0.1
1
10
190
190
200
210
220
230
210
200
180
160
140
-90
-60
-30
0
30
60
90
Latitude

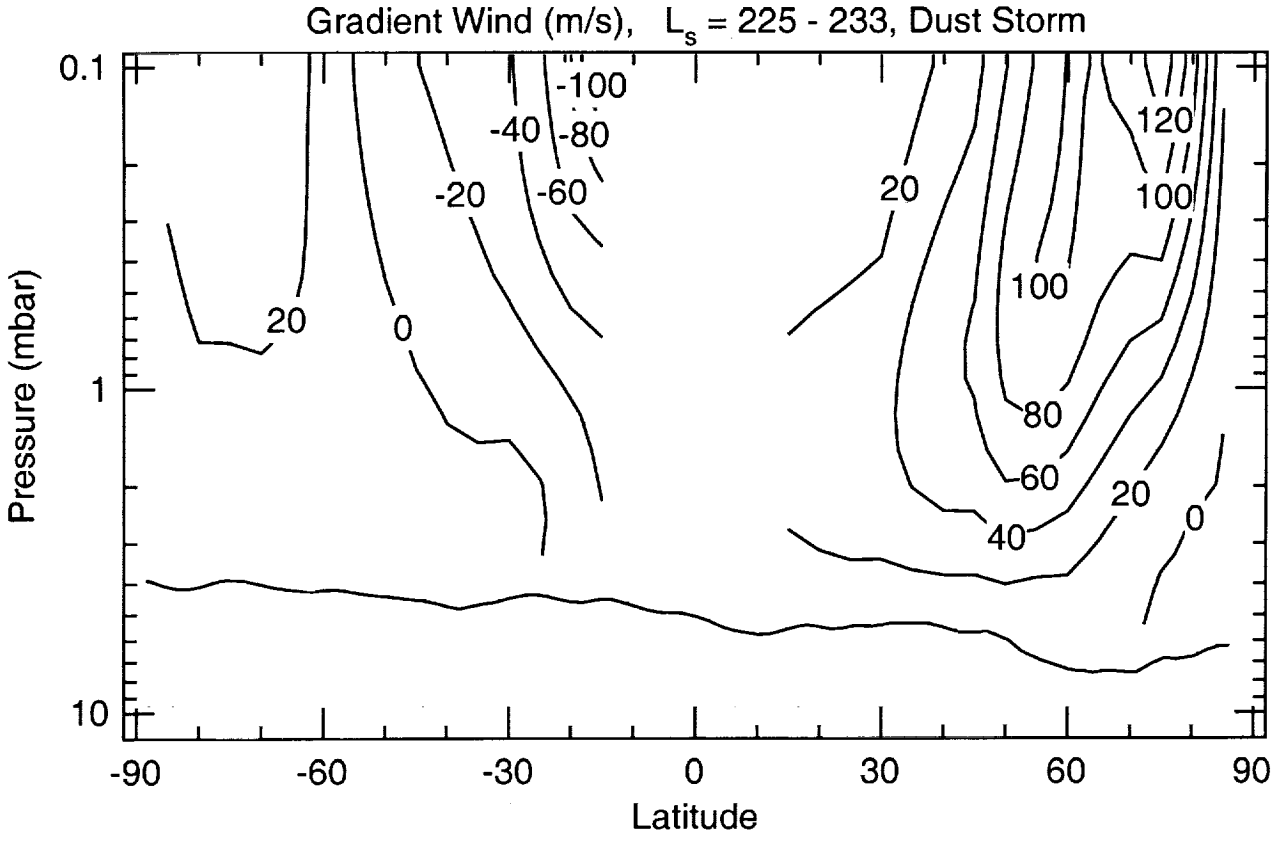
Gradient Wind (m/s), L_s = 225 - 233, Dust Storm
Pressure (mbar)
0.1
1
10
-100
-40
-80
-20
-60
20
0
20
120
100
100
80
60
40
20
0
-90
-60
-30
0
30
60
90
Latitude

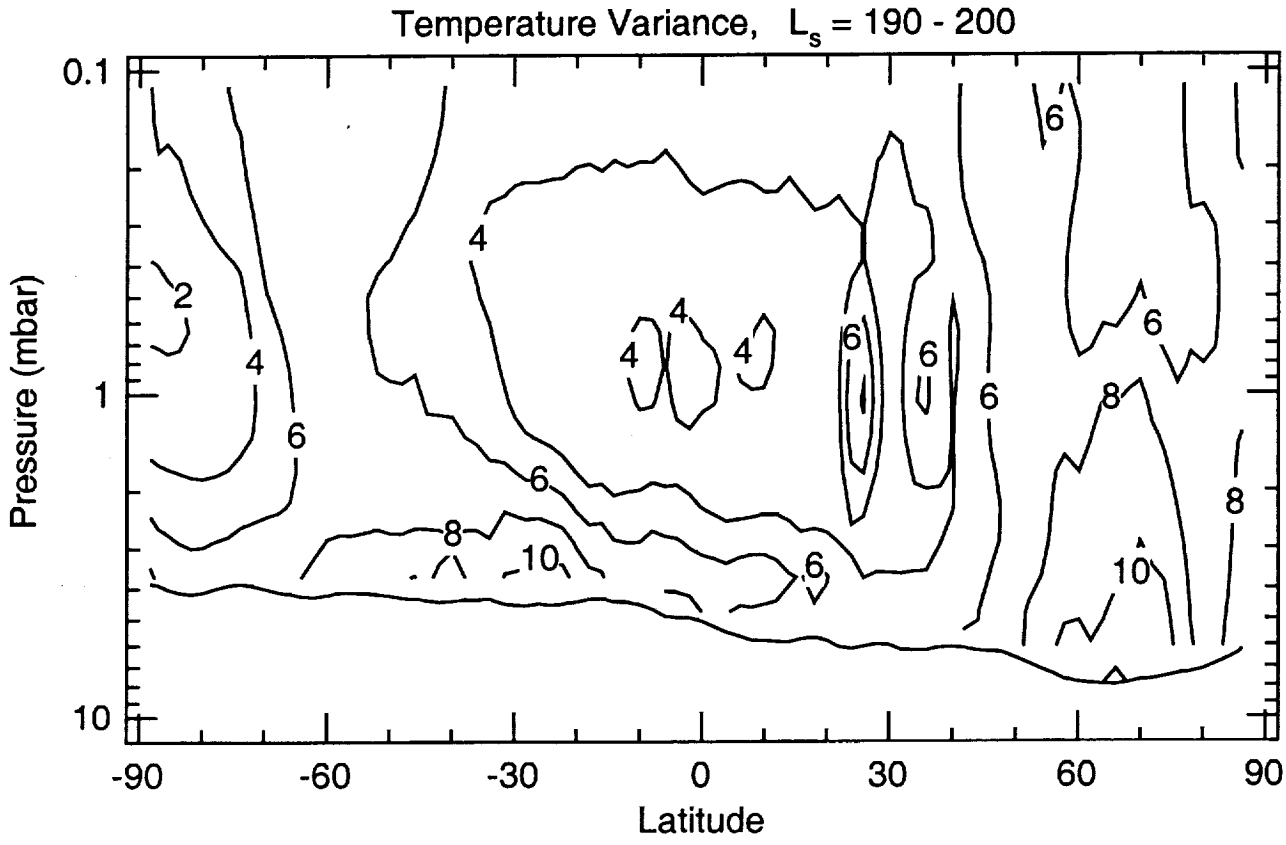
Temperature Variance, L_s = 190 - 200
Pressure (mbar)
0.1
1
10
-90
-60
-30
0
30
60
90
Latitude
2
4
6
8
10

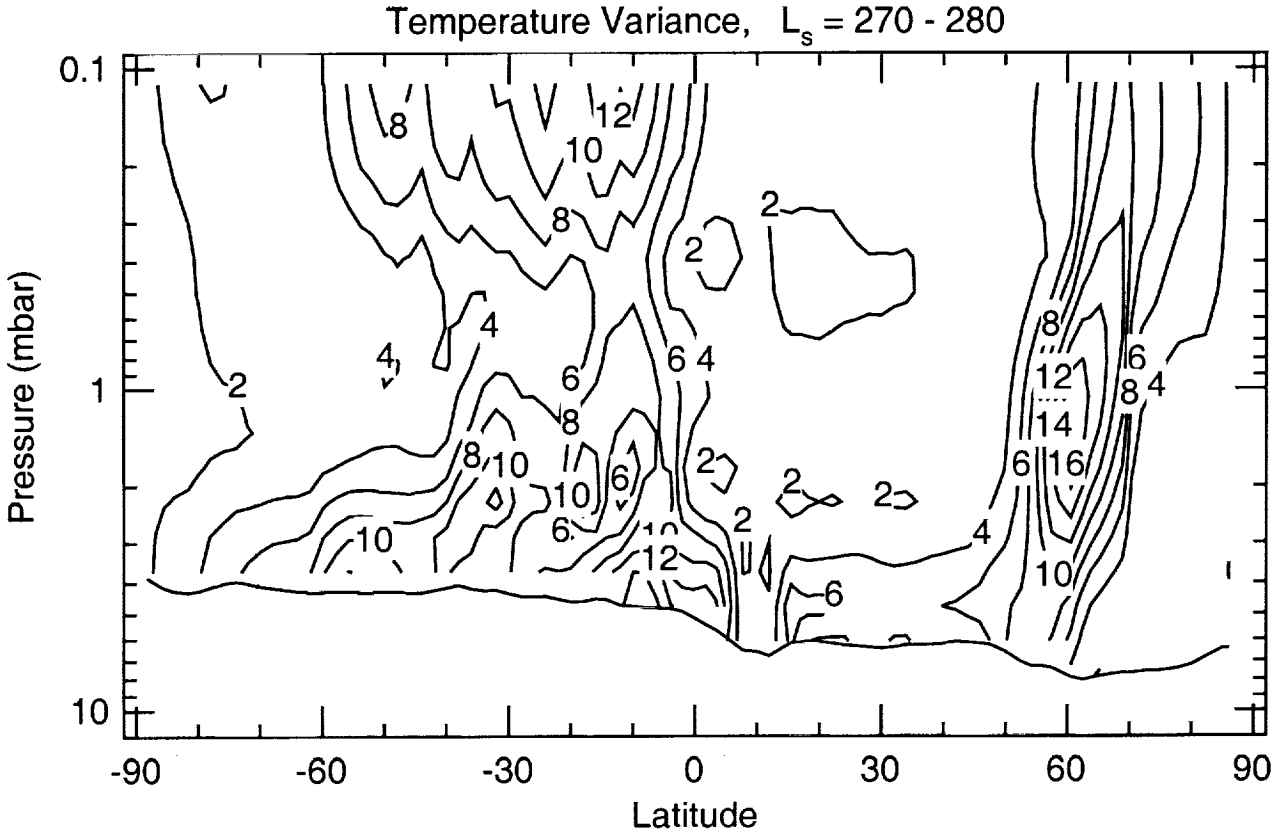
Temperature Variance, L_s = 270 - 280
Pressure (mbar)
0.1
1
10
-90
-60
-30
0
30
60
90
Latitude

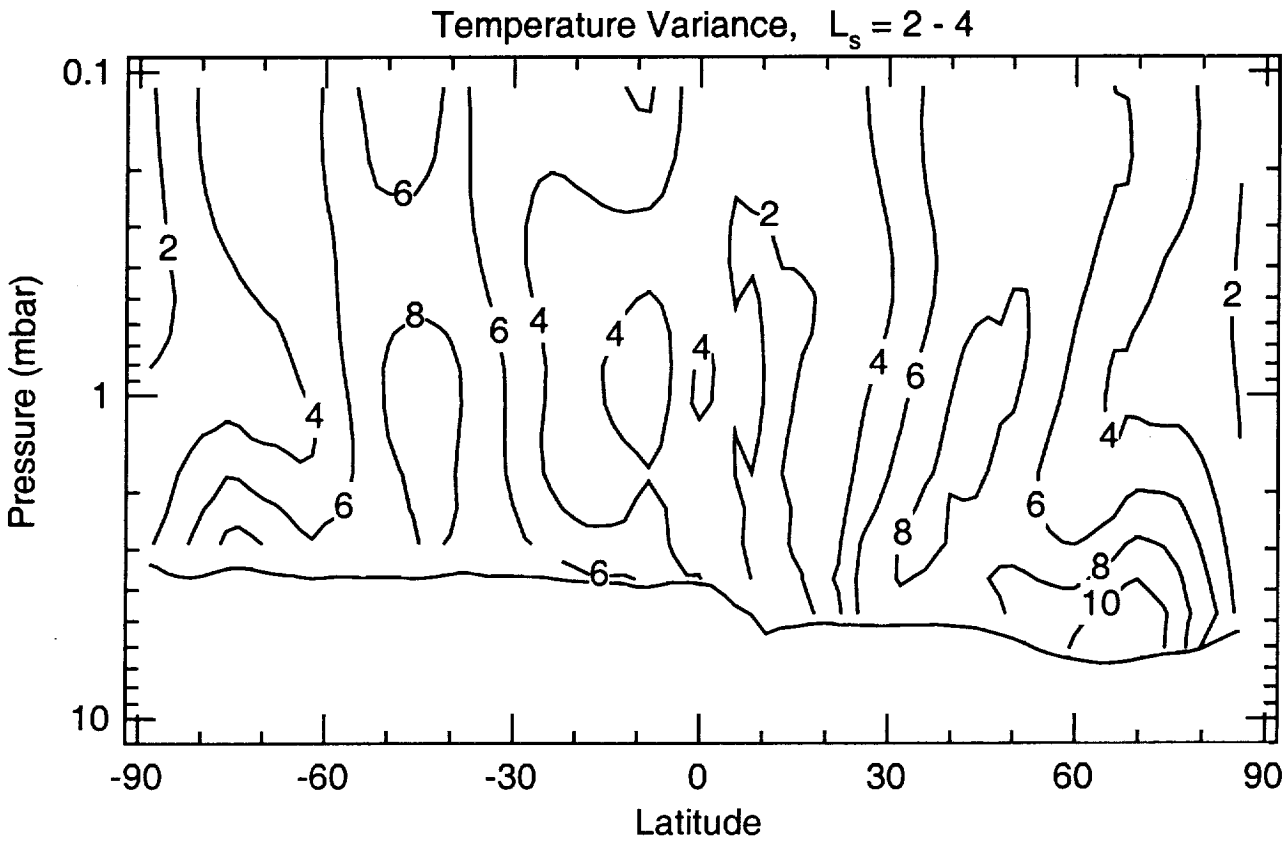
Temperature Variance, L_s = 2 - 4
Pressure (mbar)
0.1
1
10
-90
-60
-30
0
30
60
90
Latitude
2
4
6
8
10

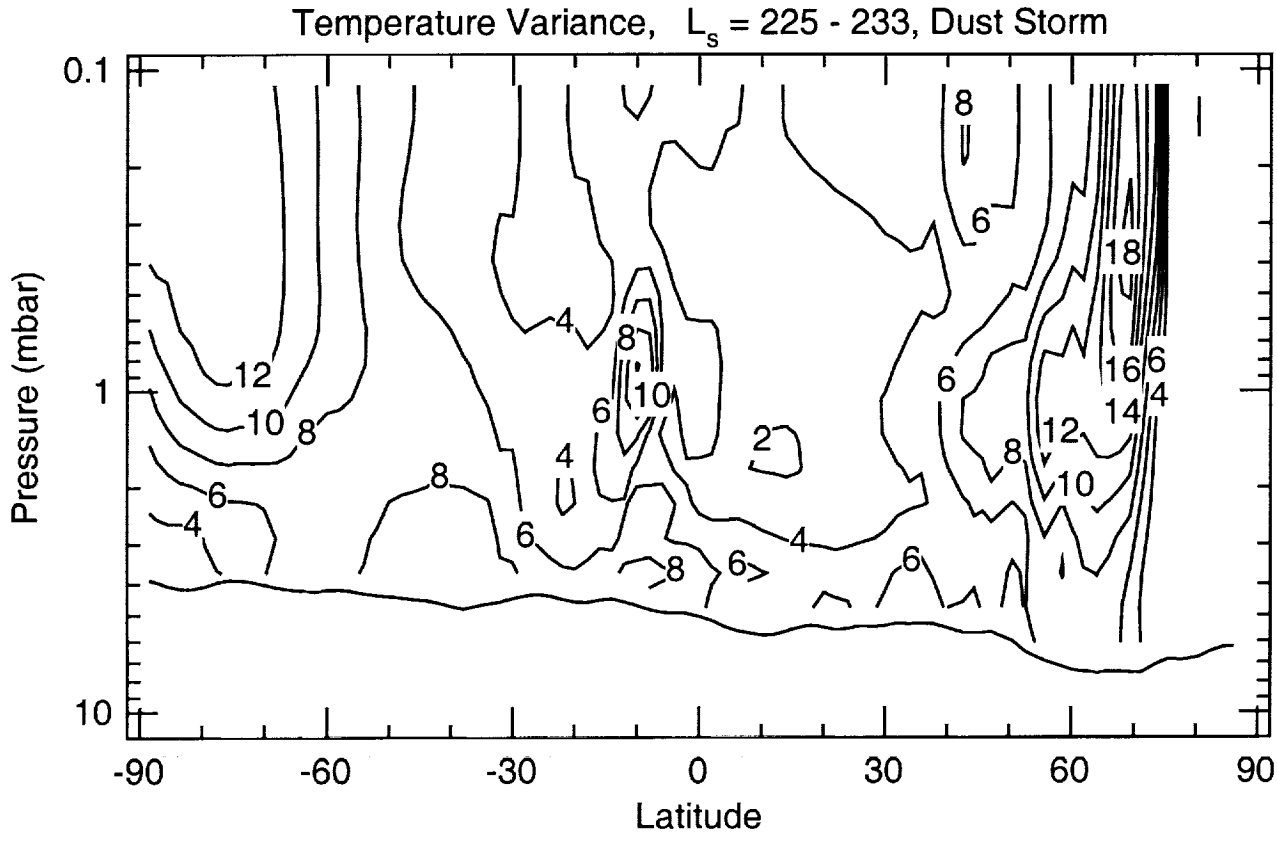
Temperature Variance, L_s = 225 - 233, Dust Storm
Pressure (mbar)
0.1
1
10
-90
-60
-30
0
30
60
90
Latitude
12
10
8
6
4
8
6
4
8
10
6
4
2
8
6
4
8
6
6
8
6
18
16
6
4
14
12
10